The Discontinuous Galerkin Material Point Method for variational hyperelastic-plastic solids

Adrien Renaud, Thomas Heuzé, Laurent Stainier

The Discontinuous Galerkin Material Point Method for variational hyperelastic-plastic solids

Adrien Renaud[1,2], Thomas Heuzé[2], Laurent Stainier[2]

[1] *Université Paris-Saclay*
CentraleSupélec, Laboratory MSSMat (UMR 8579 CNRS)
8-10 rue Joliot-Curie, 91190 Gif-sur-Yvette
e-mail: adrien.renaud@centralesupelec.fr

[2] *Laboratory GeM (UMR 6183 CNRS)*
Ecole Centrale de Nantes
1 rue de la Noë, 44300 Nantes
e-mail: {thomas.heuze,laurent.stainier}@ec-nantes.fr

Abstract

The Discontinuous Galerkin Material Point Method (DGMPM) presented in [1] is based on the discretization of a solid domain by means of particles in a background mesh. Owing to the employment of the discontinuous Galerkin approximation on the grid, the weak form of a hyperbolic system involves fluxes that are computed at cell interfaces by means of an approximate Riemann solver. Combining these fluxes with the projection of the updated solution from the nodes to the particles originally used in the Particle-In-Cell method allows a significative reduction of the numerical oscillations that pollute the classical MPM solutions. Although the DGMPM exhibits very promising aspects, such as the control of the time-stepping [2] or the ability to locally increase the approximation order in an arbitrary grid, the method first needs to be tested in its early version on problems involving a more complex wave content. It is then proposed in this paper to couple the DGMPM with variational integrators of hyperelastic-plastic constitutive models. The genericity provided for dealing with rate-indepedent or rate-dependent plasticity, as well as the possibility to easily extend the DGMPM to thermomechanical problems, makes this class of integrators appealing. The approach is here illustrated on numerical examples for which comparisons are shown with the finite element and the material point methods, as well as a one-dimensional exact solution in the linearized geometrical limit.

Keywords: Discontinuous Galerkin Material Point Method; hyperelastic-plastic solids; variational constitutive update; impacts

1. Introduction

Systems of hyperbolic conservation laws governing the propagation of mechanical waves in dissipative solids are of great interest for the numerical simulation of high-speed forming techniques or crash-proof design for instance. In these solids, whose behavior depends on history effects, the waves propagate while carrying the information about the loading, interacting with each other, and reflecting on the boundaries so that complex responses arise. The accurate assessment of irreversible deformations in dissipative solids therefore requires the correct description of those waves as well as the ability to account for their interactions. Hyperbolic problems may be further complicated by possibly large displacements, rotations or strains undergone by the solid.

For the reasons mentioned above, the simulation of such problems is not a straightforward undertaking. Indeed, the precise tracking of waves involves the use of a numerical method whose solutions are devoided of oscillations and too much numerical diffusion on the one hand, and that is able to manage large deformations on the other hand. The numerical simulation of hyperbolic initial boundary value problems in solids has been so far mostly addressed in industrial codes by using the Finite Element Method (FEM) [3]. FEM became attractive due to its ability to handle low or high-order approximations, and to easily deal with complex geometries and nonlinear constitutive models. Nevertheless, some difficulties related to the deformation of the mesh may be encountered when the formulation

is built upon a material description of the motion (Lagrangian approach). In fact, the method is less efficient and accurate when the elements are highly distorted or entangled so that re-meshing techniques and projection steps must be employed. These issues can be avoided by using a spatial description of the motion (Eulerian approach). However interface tracking techniques and diffusive convection steps are required in order to follow the boundaries and transport internal variables respectively, which is less convenient for solid mechanics. Alternatively, Arbitrary Lagrangian Eulerian (ALE) methods aim at meeting advantages of both approaches while freeing themselves of their respective limits by distinguishing the motion of the mesh to that of the material points. This type of strategy nonetheless also requires re-meshing or re-zoning procedures that can be costly for fine meshes, as well as diffusive projection steps of internal variables for solid media. In addition to problems implied by finite deformations, classical explicit time integrators used in solid dynamics with FEM introduce high frequency noise in the vicinity of discontinuities. Such regions of high gradient may be caused by discontinuous waves that can occur in the solutions of hyperbolic problems. The removal of these spurious numerical oscillations with additional viscosities is difficult to achieve without loss of accuracy, and can be troublesome for the wave tracking.

On the other hand, the Finite Volume Method (FVM) [4], initially developed for fluid dynamics, provided until the 90s piece-wise constant or piece-wise linear approximate solutions in cells that discretize a continuum. The extension to very high-order has since been proposed by increasing the stencil of the scheme (see WENO [5]). This class of methods can embed tools based on the Total Variation Diminishing (TVD) stability condition [6], thus ensuring that no spurious oscillations arise in the solutions. The formulation moreover relies on a conservative form leading to the same order of accuracy for all components of the unknown vector. In particular, one shows that both the velocity and its gradient arise in that vector for solid mechanics [7]. This makes a big difference with respect to methods that do not use a differential system of order one, namely the classical displacement-based FEM, for which the convergence rate of gradients is one order less than that of the displacement. FVM formulations moreover rely on numerical fluxes that enable to account for the characteristic structure of hyperbolic equations, thus allowing an accurate tracking of the path of waves. Recent studies extended these approaches to solid mechanics for problems involving history-dependent models [8, 9], or finite deformations with a Lagrangian formulation [7, 10]. Nevertheless, those methods are also grid-based techniques for which numerical difficulties linked to large deformations occur.

Alternatively, Particle-In-Cell methods (PIC) [11] are based on particles that move in a computational mesh while carrying the fields of a problem. The underlying grid is used in order to compute an approximate solution that is projected and stored at the particles. As a result, the background mesh can be discarded at each time step and re-constructed for computational convenience. The application of PIC to solid mechanics led to the Material Point Method (MPM) [12] in which the constitutive equations are managed at particles. Hence, the MPM can be seen as a mesh-free extension of FEM with quadrature points moving in elements. Overcoming the storage of the approximate solutions based on elements, or cells, enables the removal of mesh entanglement instabilities. Nevertheless, the projection required from the grid to the particles gives rise to some issues. As originally proposed in PIC, a classical interpolation leads to significant numerical diffusion due to a spreading of the information over several cells. Alternatively, the FLuid Implicit Particle method (FLIP) [13] makes use of a different mapping procedure that enables a reduction of the diffusion at the cost of spurious oscillations [14]. More recently, a coupling between the Discontinuous Galerkin approximation in space (DG) [15] and the MPM has been proposed in order to address the balance between numerical noise and diffusion. The DGMPM [1] thus makes use of an interpolation of updated nodal quantities to the particles (*i.e. PIC projection*), based on shape functions whose supports reduce to one cell so that the numerical diffusion is limited [16]. It then follows that the dual mesh consisting of an arbitrary grid and a set of particles allows to take advantage of both FEM and FVM. Indeed, the element-wise weak form written on the background grid involves intercell fluxes and well-known constitutive integrators [17] can be used at the material points, the mapping between the nodes and the particles being based on piece-wise linear Lagrange polynomials. The numerical solution of hyperbolic problems with the DGMPM for hyperelastic solids shows good agreements with exact solutions as well as significant improvements with respect to the original MPM [1].

Even though the DGMPM exhibits promising features that have not been exploited so far (*i.e. the ability to locally increase the approximation order in an arbitray grid, etc.*), the method is here illustrated on problems involving rate-independent elastic-plastic solids undergoing finite deformations. The purpose of that work is to better qualify the method on dissipative solids that involve a richer spectral content than purely hyperelastic materials.

More specifically, the class of hyperelastic-plastic solids is considered in this work since it falls in a thermodynamically-consistent framework, in contrast with the class of hypoelastic-plastic constitutive models. The considered thermo-

dynamic framework allows to recast the set of equations associated with hyperelastic-plastic constitutive models into a variational form [18]. On the one hand, this variational framework brings a level of genericity to the approach since it can be shown that it encompasses a lot of classes of dissipative constitutive models for solids (rate-dependent and rate-independent plasticity, viscoelasticity, damage, thermomechanical coupling etc.) [18, 19, 20, 21, 22]. This should facilitate the extension of the DGMPM to these constitutive models and to strongly thermo-mechanically coupled problems. On the other hand, effective dedicated variational integrators that make a direct use of standard minimization algorithms introduced at first in the optimization domain [23] can be used to compute the updated solution.

The outline of the paper is as follows. The continuum equations of isothermal solid dynamics including balance laws and variational constitutive equations are first recalled in section 2. Next, the derivation of the DGMPM discrete system that must be solved on the background grid at each time step is briefly recalled in section 3. The discrete system is based on the calculation of intercell fluxes by means of a hyperelastic approximate-state Riemann solver which is presented in section 4. The variational constitutive update for the integration of plastic flow at material points is recalled in section 5. At last, the method is illustrated on one and two-dimensional simulations in section 6 for which comparisons with FEM and MPM solutions are shown.

2. Continuum equations: isothermal dynamics

2.1. Conservation laws

Consider a solid domain in the initial or reference configuration $\Omega_0 \subset \mathbb{R}^3$, bounded by the surface $\partial\Omega$, in which material particles are located with Lagrange coordinates $\boldsymbol{X} = X_\alpha \boldsymbol{e}_\alpha \in \Omega_0$. The motion of the particles within the time interval $t \in \tau = [0, T^{end}]$ is governed by the following set of equations, which respectively correspond to geometrical balance laws [10, 24, 25] and the balance equation of the Lagrangian linear momentum:

$$\dot{\boldsymbol{F}} - \boldsymbol{\nabla}_0 \cdot (\boldsymbol{v} \otimes \boldsymbol{I}) = \boldsymbol{0} \quad \forall \boldsymbol{X}, t \in \Omega_0 \times \tau \tag{1}$$

$$\rho_0 \, \dot{\boldsymbol{v}} - \boldsymbol{\nabla}_0 \cdot \boldsymbol{\Pi} = \rho_0 \boldsymbol{b} \quad \forall \boldsymbol{X}, t \in \Omega_0 \times \tau \tag{2}$$

In the above set, $\boldsymbol{I}$, $\boldsymbol{F}$ and $\boldsymbol{\Pi}$ are the second-order identity, the deformation gradient and the first Piola-Kirchhoff stress tensors, $\boldsymbol{v}$ is the velocity vector and $\boldsymbol{\nabla}_0 \cdot (\bullet)$ is the divergence operator in the reference configuration. Moreover, $\rho_0(\boldsymbol{X})$ and $\boldsymbol{b}(\boldsymbol{X}, t)$ denote the reference mass density and the body forces vector respectively. From now on, calligraphic symbols stand for column arrays and the body forces are neglected.

Introduction of the vector of conserved quantities $\mathcal{U} = [\rho_0 \boldsymbol{v} \, , \, \boldsymbol{F}]$ allows the writing of a system of conservation laws consisting of equations (1) and (2):

$$\frac{\partial \mathcal{U}}{\partial t} + \boldsymbol{\nabla}_0 \cdot \mathcal{F} = \boldsymbol{0} \quad \forall \boldsymbol{X}, t \in \Omega_0 \times \tau \tag{3}$$

where $\mathcal{F} = -[\boldsymbol{\Pi} \, , \, \boldsymbol{v} \otimes \boldsymbol{I}]$ is the flux vector. In Cartesian coordinates, system (3) reads:

$$\frac{\partial \mathcal{U}}{\partial t} + \frac{\partial \mathcal{F} \cdot \boldsymbol{e}_\alpha}{\partial X_\alpha} = \boldsymbol{0} \quad \forall \boldsymbol{X}, t \in \Omega_0 \times \tau \tag{4}$$

with $\mathcal{F} \cdot \boldsymbol{e}_\alpha = -[\boldsymbol{\Pi} \cdot \boldsymbol{e}_\alpha \, , \, \boldsymbol{v} \otimes \boldsymbol{e}_\alpha]$. Alternatively, the use of an auxiliary vector $\mathcal{Q} = [\boldsymbol{v} \, , \, \boldsymbol{\Pi}]$, along with the chain rule, leads to the following quasi-linear form [26]:

$$\frac{\partial \mathcal{Q}}{\partial t} + \mathbf{J}^\alpha_{\mathcal{Q}} \frac{\partial \mathcal{Q}}{\partial X_\alpha} = \boldsymbol{0} \quad \forall \boldsymbol{X}, t \in \Omega_0 \times \tau \tag{5}$$

$$\text{with } \mathbf{J}^\alpha_{\mathcal{Q}} = -\left(\frac{\partial \mathcal{U}}{\partial \mathcal{Q}}\right)^{-1} \frac{\partial \mathcal{F} \cdot \boldsymbol{e}_\alpha}{\partial \mathcal{Q}} = -\begin{bmatrix} \boldsymbol{0}^2 & \frac{1}{\rho_0} \boldsymbol{I} \otimes \boldsymbol{e}_\alpha \\ \frac{\partial \boldsymbol{\Pi}}{\partial \boldsymbol{F}} \cdot \boldsymbol{e}_\alpha & \boldsymbol{0}^4 \end{bmatrix}$$

in which $\boldsymbol{0}^k$ denotes a kth-order zero tensor. The constitutive model of the material is then explicitly involved in the quasi-linear form through the fourth-order tangent modulus tensor $\mathbb{H} = \frac{\partial \boldsymbol{\Pi}}{\partial \boldsymbol{F}}$.

2.2. Constitutive model: Hyperelastic-plastic materials

Following the multiplicative decomposition of the deformation gradient [27]: $\boldsymbol{F} = \boldsymbol{F}^e\boldsymbol{F}^p$, irreversible processes that account for the evolution of the micro-structure of the material are described by means of internal variables [28]. Denoting by $\mathcal{V}$ the column array consisting of hardening variables, the complete set of internal variables is: $\{\boldsymbol{F}^p, \mathcal{V}\}$. It is assumed that the evolution of internal variables only depends on the local state, so that the kinetic equations can be written:

$$\dot{\mathcal{V}} = f(\boldsymbol{F}, \boldsymbol{F}^p, \mathcal{V})$$

For the sake of simplicity, isotropic and kinematic hardenings are considered here. In that case, the array $\mathcal{V}$ consists of the cumulated plastic strain p and the plastic flow rule reads:

$$\dot{\boldsymbol{F}}^p\boldsymbol{F}^{p-1} = \dot{p}\boldsymbol{M} \tag{6}$$

In equation (6), kinematic conditions for the plastic flow are prescribed through the second-order tensor $\boldsymbol{M}$. More specifically, the von Mises flow rule results from the restriction $\boldsymbol{M} \in \{\boldsymbol{A} \in \mathbb{R}^3 \times \mathbb{R}^3 \mid \boldsymbol{A} : \boldsymbol{A} = \frac{2}{3},\ \boldsymbol{A} : \boldsymbol{I} = 0\}$.

For materials in which internal processes do not influence the elastic response (*e.g. metals*), the thermodynamic state is described by the Helmholtz free energy density that is assumed to decompose additively as:

$$\psi(\boldsymbol{F}, \boldsymbol{F}^p, p) = \psi^e(\boldsymbol{F}\boldsymbol{F}^{p-1}) + \psi^p(\boldsymbol{F}^p, p)$$

where ψ^e and ψ^p govern elastic and plastic evolutions respectively. The partial derivatives of the free energy density yield [29]:

$$\boldsymbol{\Pi} = \frac{\partial\psi}{\partial\boldsymbol{F}} \quad ; \quad \boldsymbol{T} = -\frac{\partial\psi}{\partial\boldsymbol{F}^p} \quad ; \quad Y = -\frac{\partial\psi}{\partial p}$$

where $\boldsymbol{\Pi}$ is the first Piola-Kirchhoff stress tensor, $\boldsymbol{T} = \boldsymbol{F}^{eT}\boldsymbol{\Pi} - \boldsymbol{\Xi}$, $\boldsymbol{\Xi}$ being the back-stress tensor, and Y is the force thermodynamically conjugate to the cumulated plastic strain.

Considering the plastic flow rule (6), we can write the dissipation

$$\boldsymbol{\Pi} : \dot{\boldsymbol{F}} - \dot{\psi} = \boldsymbol{T} : \dot{\boldsymbol{F}}^p + Y\dot{p} = \left((\boldsymbol{T}\boldsymbol{F}^{pT}) : \boldsymbol{M} + Y\right)\dot{p} = \hat{Y}\dot{p}$$

We then postulate the existence of a pseudo-dissipation potential ϕ from which the rate of the cumulated plastic strain can be derived:

$$\dot{p} = \frac{\partial\phi(\hat{Y})}{\partial\hat{Y}}$$

Alternatively, the dual pseudo-dissipation potential $\phi^*(\dot{p})$, that results from the Legendre transform of ϕ:

$$\phi^*(\dot{p}) = \sup_{\hat{Y}}\left\{\hat{Y}\dot{p} - \phi(\hat{Y})\right\} \tag{7}$$

allows writing:

$$\hat{Y} = \frac{\partial\phi^*(\dot{p})}{\partial\dot{p}} \tag{8}$$

2.3. Variational formulation of the constitutive model

The above constitutive equations are usually integrated within an incremental procedure by means of return mapping algorithms [17]. The set of equations can also be formulated as an optimization problem by introducing some power density function [18, 22]:

$$\mathscr{P}(\dot{\boldsymbol{F}}, \dot{p}) = \dot{\psi} + \phi^*(\dot{p}) = \frac{\partial\psi}{\partial\boldsymbol{F}} : \dot{\boldsymbol{F}} - \hat{Y}\dot{p} + \phi^*(\dot{p})$$

whose minimizations with respect to $\dot{p}$ and $\boldsymbol{M}$ respectively lead to:

$$-\hat{Y} + \frac{\partial\phi^*}{\partial\dot{p}} = 0 \quad ; \quad \max_{\boldsymbol{M}}\{\boldsymbol{T}(\boldsymbol{M}\boldsymbol{F}^p) \cdot \dot{p}\}$$

The first equation is the dual form of the kinetic equations (8) while the second one yields the determination of the plastic flow direction by satisfying the principle of maximum plastic dissipation. Moreover, it can be shown that the effective power density $\mathscr{P}^{eff}(\dot{\boldsymbol{F}}) = \min_{\dot{p},\boldsymbol{M}} \mathscr{P}$ acts as a rate potential for $\boldsymbol{\Pi}$, that is:

$$\boldsymbol{\Pi} = \frac{\partial \mathscr{P}^{eff}}{\partial \dot{\boldsymbol{F}}}$$

Such a recasting of the equations, combined with the approximation of $\mathscr{P}^{eff}$ over a time increment, enables the construction of variational constitutive updates for which the constitutive model appears as *pseudo-hyperelastic*. This will be the object of section 5.

3. DGMPM discrete equations

The continuum body Ω is discretized into a set of N_p material points in an arbitrary Cartesian grid made of N_n nodes and E non-overlapping cells of volume Ω^e (a two-dimensional example is depicted in figure 1).

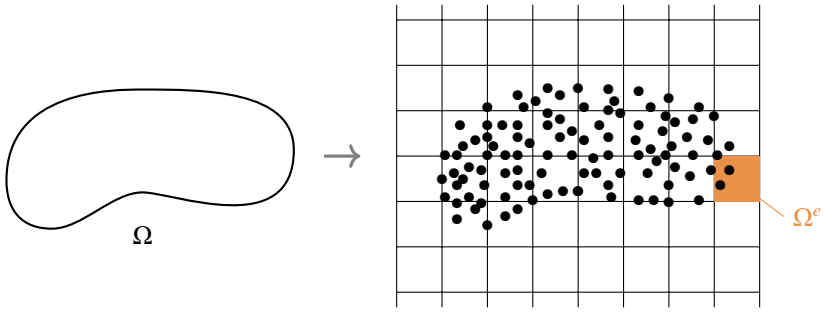

Figure 1: Discretization of a two-dimensional solid domain using particles in an arbitrary grid.

One central point of the DGMPM, which is inherited from the original MPM [12, 30], is the use of a particle-based definition of the mass density on the grid by means of Dirac delta function:

$$\rho_0(\boldsymbol{X}) = \sum_{p=1}^{N_p} m_p \delta(\boldsymbol{X}^p - \boldsymbol{X}), \tag{9}$$

along with specific fields:

$$\mathcal{U} = \rho_0 \bar{\mathcal{U}} \quad ; \quad \mathcal{F}_\alpha = \rho_0 \bar{\mathcal{F}}_\alpha \tag{10}$$

Following [1], the discontinuous Galerkin approximation allows writing an element-wise weak form of equation (3) on the grid. The volume integrals of that weak form next transform to discrete sums over the material points by introducting the specific fields (10), combined with the definition (9). The following total Lagrangian weak formulation is then written:

$$\sum_{p=1}^{N_p} m_p \left[\frac{\partial \bar{\mathcal{U}}}{\partial t} \mathcal{W} - \bar{\mathcal{F}}_\alpha \frac{\partial \mathcal{W}}{\partial X_\alpha} \right]_{|\boldsymbol{X}=\boldsymbol{X}^p} + \int_{\partial\Omega^e} \mathcal{F}_N \mathcal{W} \, dS = 0 \quad \forall \, \mathcal{W}, e \tag{11}$$

In equation (11), $\partial\Omega^e$ is the boundary of the eth element with outward normal vector $\boldsymbol{N}$ and $\mathcal{W}$ is a test function belonging to the same broken polynomial space as $\bar{\mathcal{U}}$ [31].

In a similar manner to FEM [3] and MPM [12], the fields are approximated on the mesh as:

$$\mathcal{A}(\boldsymbol{X}, t) = \sum_{i=1}^{N_n} S_i(\boldsymbol{X}) \mathcal{A}^i(t) \tag{12}$$

where $\mathcal{A}^i$ denotes a generic quantity evaluated at node i, and $S_i(\boldsymbol{X})$ the (linear) shape function attached to it. Note that particle and nodal quantities are respectively denoted with p and (i, j) subscripts or superscripts.

Introduction of the DGMPM approximation (12) within the weak form (11) yields the semi-discrete system:

$$\sum_{p=1}^{N_p}\left[S_{ip}m_pS_{jp}\frac{\partial\bar{\mathfrak{U}}^j}{\partial t}-\frac{\partial S_{ip}}{\partial X_\alpha}m_pS_{jp}\bar{\mathfrak{F}}^j_\alpha\right]+\int_{\partial\Omega^e}S_i(\boldsymbol{X})\mathfrak{F}_N\,dS=0\quad\forall\, e$$

or, in matrix form:

$$M_{ij}\frac{\partial\bar{\mathfrak{U}}^j}{\partial t}-K^\alpha_{ij}\bar{\mathfrak{F}}^j_\alpha+\hat{\mathfrak{F}}^i=\mathbf{0}$$

As already highlighted in [1], the diagonally lumped mass matrix: $M^L_{ij}=\sum_k M_{ik}\delta_{ij}$, can be used in place of the consistent mass matrix that can be singular due to the particle-based integration. Alternatively, an effective mass matrix was introduced in [32] as the convex combination of the consistent and the lumped matrices. Nevertheless, the aforementioned mass matrix involves an additional parameter according to its definition: $\widetilde{M}_{ij}=\xi\,M^L_{ij}+(1-\xi)M_{ij}$, with $\xi\in[0,1]$. As we shall discuss in section 6, no value of ξ is recommended in the MPM literature so that its choice lets some freedom.

At last, the discrete system, which is solved at nodes, is derived by discretizing the time interval τ into N_t subintervals and using the explicit forward Euler method. Since, the loading history is stored at material points, a reconstruction of the fields from the particles to the grid is required as well as a projection of the updated solution from the grid to the material points. The reconstruction procedure is similar to that used within the MPM and consists in ensuring the conservation of volume quantities by solving for the $\bar{\mathfrak{U}}^{i,n}$:

$$\widetilde{M}_{ij}\bar{\mathfrak{U}}^{i,n}=\sum_{p=1}^{N_p}S_{jp}m_p\bar{\mathfrak{U}}^{p,n}\quad\text{for } i=1,...,N_n \tag{13}$$

The back-mapping follows that proposed in the Particle-In-Cell method (PIC) [11], namely, a classical interpolation:

$$\bar{\mathfrak{U}}^{p,n+1}=\sum_{i=1}^{N_n}S_{ip}\bar{\mathfrak{U}}^{i,n+1}$$

Notice that the MPM uses a different projection from nodes to particles that was introduced in the FLuid Implicit Particle method (FLIP) [33]. The FLIP mapping reduces the numerical diffusion resulting from the interpolation used in PIC at the cost of spurious oscillations. The employment of the PIC projection rather than the FLIP one within the DGMPM is motivated by the willingness to avoid oscillations that can, for plastic materials, lead to a premature plastic flow due to overshoots. On the other hand, the diffusion inherent in PIC mapping is expected to be less significant with discontinuous shape functions owing to the reduction of the domain of influence of nodes during the projection steps.

4. Computation of intercell fluxes

DG methods for hyperbolic problems are based on the requirement of ensuring monotonicity of the scheme for piecewise constant approximations [34]. Such approaches are monotone for flux functions $\mathfrak{F}_N$ that are Lipschitz continuous, consistent and monotone, namely, they must be E-fluxes [35]. One possibility, which is widely used and adopted here, is the Godunov flux function.

Let us consider the following Riemann problem defined at the interface between two DGMPM cells having normal vector $\boldsymbol{N}$:

$$\begin{aligned}&\frac{\partial\mathfrak{U}}{\partial t}+\frac{\partial\mathfrak{F}_N}{\partial X_N}=\mathbf{0},\quad X_N=\boldsymbol{X}\cdot\boldsymbol{N}\\&\mathfrak{U}(X_N,0)=\begin{cases}\mathfrak{U}_{X_N^-}\text{ if } X_N<0\\\mathfrak{U}_{X_N^+}\text{ if } X_N>0\end{cases}\end{aligned} \tag{14}$$

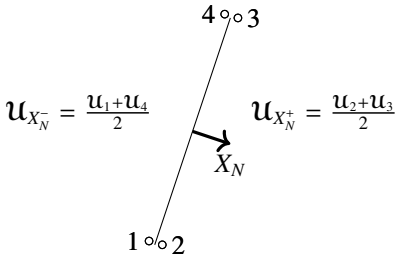

Figure 2: Duplication of nodes at an interface and building of initial conditions of the Riemann problem (2D).

The initial conditions $\mathcal{U}_{X_N^-}$ and $\mathcal{U}_{X_N^+}$ result from the average of nodal fields on each side of the interface, so that one Riemann problem is solved at each edge (see a two-dimensional example in figure 2).

The characteristic structure of the solution of problem (14) consists of waves emanating from the origin of the (X_N, t) plane [36]. The wave pattern can be determined by the spectral analysis of the Jacobian matrix: $\mathbf{J}_\mathcal{U} = \frac{\partial \mathcal{F}_N}{\partial \mathcal{U}}$. The eigenvalues c_k and associated right eigenvectors $\mathcal{R}^k$ ($k = 1, ..., D$), D being the dimension of the Jacobian, are respectively stored as diagonal entries and columns of matrices $\mathbf{C}$ and $\mathbf{R}$ which are defined as:

$$\mathbf{J}_\mathcal{U}\mathbf{R} = \mathbf{R}\mathbf{C}$$

For flux vectors that are non-linear functions of $\mathcal{U}$, as those involved for hyperelastic constitutive models, solving problem (14) drastically increases the computational cost since this requires iterative procedures. Nonetheless, linearized Riemann solvers [37] can be constructed by approximating $\mathbf{J}_\mathcal{U}$ in the vicinity of $\mathcal{U}_{X_N^-}$ and $\mathcal{U}_{X_N^+}$ by a constant matrix $\underline{\mathbf{J}}(\mathcal{U}_{X_N^-}, \mathcal{U}_{X_N^+})$. The matrix $\underline{\mathbf{J}}$ must however ensure the hyperbolicity, namely $\underline{\mathbf{J}}$ has real eigenvalues and a complete set of independent eigenvectors [36], and satisfy the consistency condition [4]:

$$\underline{\mathbf{J}}(\mathcal{U}, \mathcal{U}) = \mathbf{J}_\mathcal{U}(\mathcal{U})$$

Both conditions can be satisfied by assuming that the negative (*resp. positive*) eigenvalues and the associated right eigenvectors of $\mathbf{J}_\mathcal{U}$, which correspond to left-going (*resp. right-going*) waves, depend only on $\mathcal{U}_{X_N^-}$ (*resp. on* $\mathcal{U}_{X_N^+}$). Then, defining the matrices:

$$\underline{\mathbf{C}} = \begin{bmatrix} c_1(\mathcal{U}_{X_N^-}) & & & & & \\ & \cdots & & & & \\ & & c_I(\mathcal{U}_{X_N^-}) & & & \\ & & & c_{I+1}(\mathcal{U}_{X_N^+}) & & \\ & & & & \cdots & \\ & & & & & c_D(\mathcal{U}_{X_N^+}) \end{bmatrix}$$

$$\underline{\mathbf{R}} = \left[\mathcal{R}^1(\mathcal{U}_{X_N^-}),\ \ldots,\ \mathcal{R}^I(\mathcal{U}_{X_N^-}),\ \mathcal{R}^{I+1}(\mathcal{U}_{X_N^+}),\ \ldots,\ \mathcal{R}^D(\mathcal{U}_{X_N^+})\right]$$

in which $c_1 < \cdots < c_I < c_{I+1} < \cdots < c_D$, the following approximation fulfills the requirements provided that $\mathbf{J}_\mathcal{U}$ ensures the hyperbolicity:

$$\underline{\mathbf{J}} = \underline{\mathbf{R}}\,\underline{\mathbf{C}}\,\underline{\mathbf{R}}^{-1}$$

Though approximate-flux Riemann solvers, which extract information for flux functions, have been applied to hyperelastic solids (see Osher's solver in [10, 7] or the HLLC solver in [38]), the approximate-state Riemann solver is considered here. The procedure then consists in computing the stationary solution of the linearized Riemann problem as [37]:

$$\mathcal{U}^* = \mathcal{U}_{X_N^-} + \sum_{\substack{k=1 \\ c_k<0}}^{D} \delta_k \mathcal{R}^k = \mathcal{U}_{X_N^+} - \sum_{\substack{k=1 \\ c_k>0}}^{D} \delta_k \mathcal{R}^k \tag{15}$$

where the δ_k are wave strength coefficients related to the kth wave of the characteristic structure. These coefficients can be calculated by rearranging equation (15) as:

$$\mathcal{U}_{X_N^+} - \mathcal{U}_{X_N^-} = \sum_{k=1}^{D} \delta_k \mathcal{R}^k$$

so as to compute the stationary solution. Once $\mathcal{U}^*$ is known, the intercell flux is determined as $\mathcal{F}_N(\mathcal{U}^*)$ according to Godunov's method [39]. Since the vector of conserved quantities $\mathcal{U}$ contains the deformation gradient and the linear momentum while the flux consists of the stress and the velocity, the integration of constitutive equations is needed, which may be costly. This can however be avoided by solving the Riemann problem based on the quasi-linear form (5), which involves the velocity and the stress. Thus, an approximate-state Riemann solver must be built upon the linearized Jacobian matrix related to the quasi-linear form:

$$\underline{\mathbf{J}}_{\mathfrak{Q}} = \underline{\mathbf{R}}_{\mathfrak{Q}}\, \underline{\mathbf{C}}\, \underline{\mathbf{R}}_{\mathfrak{Q}}^{-1}$$

where $\underline{\mathbf{R}}_{\mathfrak{Q}}$ is the approximate matrix of the right eigenvectors of the Jacobian matrix associated with the quasi-linear form. The stationary solution of the Riemann problem then reads:

$$\mathfrak{Q}^* = \mathfrak{Q}_{X_N^-} + \sum_{\substack{k=1 \\ c_k<0}}^{D} \delta_k \mathcal{R}_{\mathfrak{Q}}^k = \mathfrak{Q}_{X_N^+} - \sum_{\substack{k=1 \\ c_k>0}}^{D} \delta_k \mathcal{R}_{\mathfrak{Q}}^k$$

in which the wave strength coefficients can be computed as:

$$\mathfrak{Q}_{X_N^+} - \mathfrak{Q}_{X_N^-} = \sum_{k=1}^{D} \delta_k \mathcal{R}_{\mathfrak{Q}}^k$$

Therefore, the auxiliary stationary state $\mathfrak{Q}^*$ enables the direct calculation of intercell fluxes. Notice however that this approach requires the projection of the velocity and the strain along with the stress from the material points to the nodes by means of the reconstruction (13).

Remark 1. *As seen in section 2, the fourth-order tangent modulus tensor arises in the Jacobian matrix of the quasi-linear form. This tensor is responsible for a more complex characteristic structure when plastic flow occurs since one has to take into account both elastic and plastic waves. For small strain problems, the corresponding characteristic structure is known in particular cases so that dedicated Riemann solvers have been developed for one-dimensional media [9] or for combined longitudinal and torsional stress loadings [40]. Given the mathematical complexity introduced by large strains, such solvers cannot be considered for finite deforming solids so far. As a result, a purely reversible evolution is commonly considered for the computation of intercell fluxes, followed by the integration of the plastic flow by using a return mapping algorithm in finite volume simulations (see [41, 42] for hypoelastic-plastic materials and [7] for hyperelastic-plastic ones). A similar approach is adopted here in such a way that the DGMPM scheme consists in a predictor-corrector procedure, the integration of the plastic flow being carried out through variational constitutive updates, which is the object of section 5.*

Remark 2. *The above method of computing the intercell fluxes can be seen as the Donor-Cell Upwind (DCU) method [4]. Alternatively, the Corner Transport Upwind (CTU) method [43], which consists in considering contributions propagating in bias and coming from upwind cells sharing only a node (in two dimensions) with another, can be used easily for edge-constant fluxes [1, 2]. This approach allows improving the stability of the numerical scheme, especially for solid mechanics problems for which strain components are coupled through Poisson's effect [2]. It has therefore been used for the two-dimensional numerical simulations of section 6.*

5. Variational constitutive update

Given a time increment $[t_n, t_{n+1}]$, variational constitutive updates can be constructed upon approximations of the effective power density $\mathscr{P}^{eff}$ introduced in section 2.3 by means of the incremental energy function:

$$W(\boldsymbol{F}_{n+1}; \boldsymbol{F}_n, p_n) = \min_{p_{n+1}, \boldsymbol{M}} \left\{ \psi\left(\boldsymbol{F}_{n+1}, \boldsymbol{F}_{n+1}^p, p_{n+1}\right) - \psi\left(\boldsymbol{F}_n, \boldsymbol{F}_n^p, p_n\right) + \Delta t \left\langle \phi^*\left(\dot{p}_n\right)\right\rangle \right\} \tag{16}$$

In equation (16), it is understood that the subscripts refer to time increments and that the thermodynamic state $(\boldsymbol{F}_n, \boldsymbol{F}_n^p, p_n)$, as well as the updated deformation gradient $\boldsymbol{F}_{n+1}$, are known. Moreover, $\langle \bullet \rangle$ stands for a suitable incremental approximation of the integral of the rate potential ϕ^* over the time step [44]. Thus, the plastic part of the deformation gradient results from the incremental plastic flow rule:

$$\boldsymbol{F}_{n+1}^p = \exp\left(\Delta p \boldsymbol{M}\right) \boldsymbol{F}_n^p$$

in which $\Delta p = p_{n+1} - p_n$, and $\boldsymbol{M}$ and p_{n+1} are the arguments of the optimization (16). At last, the updated first Piola-Kirchhoff stress tensor is:

$$\boldsymbol{\Pi}_{n+1} = \frac{\partial W}{\partial \boldsymbol{F}_{n+1}} \tag{17}$$

so that W appears as a potential for $\boldsymbol{\Pi}_{n+1}$. In addition, incremental tangent moduli corresponding to the variational update follow from the linearization of the above equation:

$$\mathbb{H}_{n+1} = \frac{\partial \boldsymbol{\Pi}_{n+1}}{\partial \boldsymbol{F}_{n+1}} = \left.\frac{\partial^2 W}{\partial \boldsymbol{F}^2}\right|_{t_{n+1}} + \left.\frac{\partial^2 W}{\partial \boldsymbol{F} \partial p} \frac{\partial p}{\partial \boldsymbol{F}}\right|_{t_{n+1}} \tag{18}$$

The variational constitutive update (17) at material points provides a generic framework in which the equations of hyperelastic-(visco)plastic materials are dealt with as those of hyperelasticity. Moreover, the thermodynamically-consistent formulation, though applied here to isothermal problems, enables the consideration of strongly thermo-mechanically coupled cases [21, 22].

Remark 3. *Note that, as in [1], a purely hyperelastic approximate Riemann solver is considered by only taking into account the first term of the right-hand side in equation* (18) *for the computation of intercell fluxes. However, while analytical expressions of the the Helmholtz free energy density were used in founding paper of the DGMPM, linearized tangent moduli are employed here. This aspect should have an impact on the approximate Riemann solver since it leads to slightly different characteristic structures. It is the object of the next section to verify whether this approximation is satisfactory with numerical simulations.*

6. Numerical results

The DGMPM is now illustrated on numerical examples considering a constitutive model based on the Hencky hyperelastic-plastic potential presented in [19] and an isotropic hardening. The values of the material parameters used are gathered in table 1, the elastic behavior being given by Young's modulus E and Poisson's ratio ν. In addition, the plastic flow is governed by the yield stress in tension σ^y and the hardening coefficient H for a linear hardening, supplemented with the power law exponent $1/n$ for a non linear hardening.

Sections 6.1 and 6.3: steel		Section 6.2: copper	
$E = 2.00 \times 10^{11}$ Pa	$\sigma^y = 4.00 \times 10^8$ Pa	$E = 1.17 \times 10^{11}$ Pa	$\sigma^y = 4.00 \times 10^8$ Pa
$\nu = 0.30$	$H = 1.00 \times 10^9$ Pa	$\nu = 0.35$	$H = 1.00 \times 10^8$ Pa
$\rho_0 = 7800\ \mathrm{kg.m^{-3}}$	$n = 10$	$\rho_0 = 8930\ \mathrm{kg.m^{-3}}$	

Table 1: Material parameters.

On the other hand, the simulations carried out with the particle-based methods, and presented in the section, employ the effective mass matrix defined in section 3, which requires the setting of the parameter ξ. Most of MPM computations that can be found in the literature are performed with a lumped mass matrix [12, 30, 45, 46, 47], in such a way that no value of the parameter ξ is recommended. The same goes for the critical Courant number which is usually set to CFL = 0.5 or CFL = 0.7, though it is not proofed mathematically since no stability analysis of the scheme exists. Contrariwise, the stability analysis of the DGMPM using the lumped mass matrix in one and two space dimensions [1, 2] provides the optimal CFL number for a given distribution of material points. It furthermore appears that the value of the critical Courant number also corresponds to a good choice for the parameter ξ in order

to balance the numerical diffusion and the stability. As a result, the CFL values given in the following stand for ξ as well in DGMPM computations. On the other hand, the Courant number used in MPM simulations is set to CFL = 0.5 while the parameter ξ is identical to this used in the DGMPM for comparison purposes. The values of the algorithmic parameters CFL and ξ used in the simulations presented below are summarized in table 2. At last, the MPM discrete systems are here solved in the reference configuration in order to avoid the grid-crossing error [48] though such a total Lagrangian formulation of the method does not appear in the literature to our knowledge.

	Section 6.1		Section 6.2		Section 6.3	
	CFL	ξ	CFL	ξ	CFL	ξ
FEM	1		0.9		0.9	
MPM(1ppc)	0.5	1	0.5	1	0.5	1
MPM(2ppc)	0.5	0.5				
MPM(4ppc)			0.5	0.4	0.5	0.4
DGMPM(1ppc)	1	1	1	1	0.95	1
DGMPM(2ppc)	0.5	0.5				
DGMPM(4ppc)			0.4	0.4	0.4	0.4

Table 2: Algorithmic parameters used in MPM and DGMPM simulations.

Remark 4. *The DG approximation leads to element-wise mass matrices, namely, a block-diagonal mass matrix, whose inversion is straightforward. This therefore enables a notable decrease in the computational time compared to the MPM. Note also that the adopted total Lagrangian framework allows a single computation of mass matrices at the beginning of the computation rather than one at each time step as required in the updated Lagrangian formulation of the method.*

6.1. Plane wave problem

Let us first look at the response of an infinite medium in directions $\boldsymbol{e}_2$, $\boldsymbol{e}_3$, and of length $l = 1\ m$ in direction $\boldsymbol{e}_1$, submitted to Riemann-type initial conditions defined on the velocity: $v_1 = v_d > 0$ for $X \in [0, l/2[$ and $v_1 = -v_d$ for $X \in]l/2, l]$. Initially, the solid is in a free stress state and the velocity is set so that plastic flow occurs:

$$v_d = \beta \frac{Y_H}{\rho c_L}$$

where $\beta > 1$ is a loading parameter, $Y_H = (\lambda + 2\mu)\sigma^y/2\mu$ denotes the Hugoniot elastic limit, $c_L = \sqrt{(\lambda + 2\mu)/\rho}$ is the elastic pressure wave speed, and (λ, μ) are Lamé's constants. Both ends of the medium are traction free and the initial setting is assumed to give rise to a plane wave, namely:

$$\boldsymbol{F} = F\boldsymbol{e}_1 \otimes \boldsymbol{e}_1 + \boldsymbol{e}_2 \otimes \boldsymbol{e}_2 + \boldsymbol{e}_3 \otimes \boldsymbol{e}_3$$
$$\boldsymbol{\Pi} = \Pi_L \boldsymbol{e}_1 \otimes \boldsymbol{e}_1 + \Pi_T \left(\boldsymbol{e}_2 \otimes \boldsymbol{e}_2 + \boldsymbol{e}_3 \otimes \boldsymbol{e}_3\right)$$

Comparisons between FEM, MPM and DGMPM solutions are proposed on the longitudinal components of the PK1 stress and the Green-Lagrange plastic strain $\boldsymbol{E}^p = \frac{1}{2}\left(\boldsymbol{F}^{pT}\boldsymbol{F}^p - \boldsymbol{I}\right)$. Linear elements and a lumped mass matrix are used within FEM with no artificial viscosity added, and the regular mesh is built so that Gauss' points are consistent with the particles, the solid being discretized with 100 finite elements or particles. The space discretization used within the MPM and the DGMPM can be based on either one single particle centered in every cell, or two particles in each element that are placed symmetrically with respect to the center. The aforementioned discretizations are respectively referred to as 1ppc and 2ppc, ppc standing for point per cell. It is in addition noteworthy that all numerical methods make use of the same variational constitutive update.

The parameter β is first set to 1.2 so that the problem falls within the linearized geometrical limit $\left\|\frac{\partial \boldsymbol{u}}{\partial \boldsymbol{X}}\right\| \ll 1$, $\boldsymbol{u}$ being the displacement vector. Then, considering a linear isotropic hardening, the computed hyperelastic-plastic solution

should tend to an exact solution analogous to that derived in [9]. The latter consists of two elastic compression waves propagating left-ward and right-ward, each followed by one plastic discontinuity. The incident elastic disturbances then reflect as unloading waves on both free boundaries and interact with each other at the center of the medium, which leads to tensile plastic reloading. In figure 3, the numerical solutions provided by the DGMPM, the MPM and the FEM are compared to the exact solution of the small strain problem in the right half of the domain, given the symmetry of the stress and the plastic strain fields.

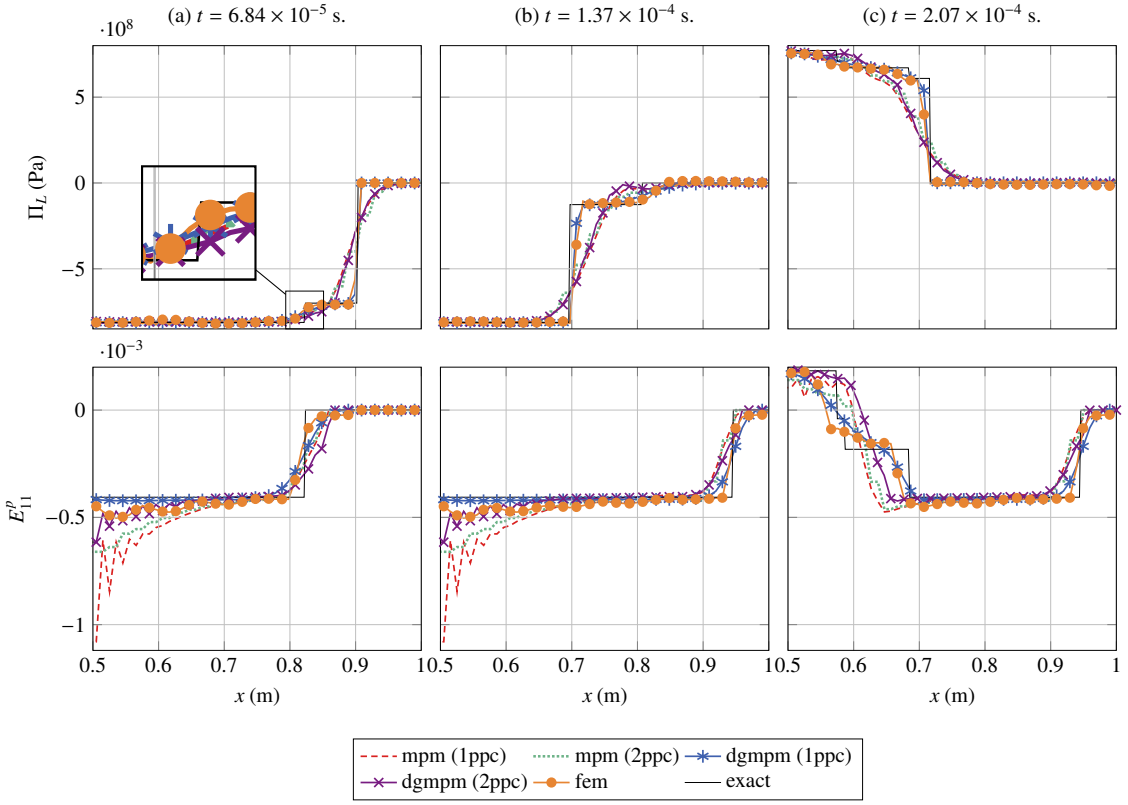

Figure 3: Longitudinal components of the PK1 stress and the plastic Green-Lagrange strain tensors along a one-dimensional hyperelastic-plastic domain subject to Riemann-type initial conditions on the velocity, plotted at different times. Comparison between FEM, MPM, DGMPM, and the exact solution of the small strain problem.

First, the incident elastic compression waves are well described by the FEM and the DGMPM using 1ppc due to the Courant number that can be set to unity [1], which is not the case for the DGMPM based on 2ppc and the MPM as seen in figure 3a. It is worth noticing that, unlike for the DGMPM, the number of particles lying in cells does not have a significant influence on the MPM results, which furthermore overlap the DGMPM(2ppc) solution. The resolution of the plastic flow leads on the other hand to less sharp solutions in terms of stress and plastic strain for all numerical schemes since the plastic discontinuous waves propagate at a lower speed. Numerical plastic strains also exhibit overshoots that are due to the FLIP projection in MPM [16], to the stress oscillations on the plastic plateau in FEM, and to an overestimation of stress at the beginning of the computation which can be removed by decreasing the CFL in DGMPM(2ppc). Notice that the plastic strain overshoot in the FEM solution cannot be reduced by refining the mesh since such a refinement would not avoid stress oscillations. Similar observations can be made in figure 3b in which elastic unloading occurs. FEM and DGMPM(1ppc) stresses are rather close to the small strains exact solution, while the three other solutions are smoother near the discontinuities. Note that the same goes for the numerical plastic strains. Next, the plastic tensile reloading that results from the interaction of the unloading waves in the central region can be seen in figure 3c. Once again, FEM and DGMPM(1ppc) lead to quite similar results in terms of stress and plastic strain, which both show good agreement with the exact solution although the discontinuities are not exactly

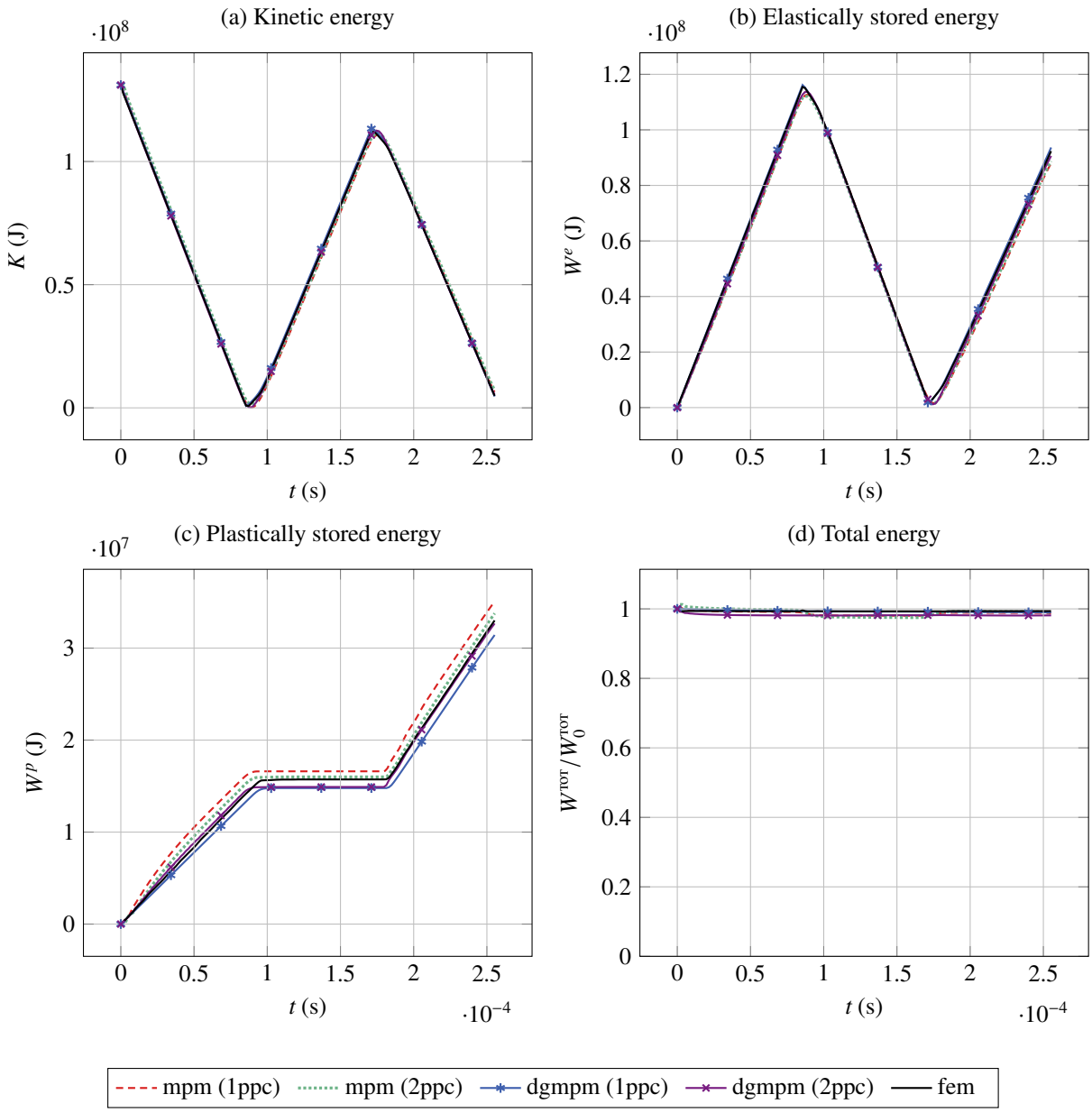

Figure 4: Evolution of energy quantities in the hyperelastic-plastic domain subject to Riemann-type initial conditions on the velocity: comparison between FEM, MPM and DGMPM solutions. Initial velocity set to $v_d = 1.2Y_H/\rho c_L$.

captured. In contrast, the stress profiles provided by the MPM and the DGMPM(2ppc) remain smooth. As a result, the corresponding plastic strains differ from the exact solution.

The evolution of energy quantities can also be seen in figure 4. First, the kinetic K, as well as the elastically stored energies W^e are depicted in figures 4a and 4b respectively. These two quantities do not show significant differences between all the numerical methods. The kinetic energy decreases before the first reflection of the incident waves on the free boundaries, which is due to the vanishing velocity upstream the elastic waves. Conversely, the elastically stored energy increases during that time interval and next decreases back until the two elastic unloading waves interact at the middle of the domain. Finally, the elastic and plastic waves resulting from the aforementioned interaction leads to a

decreasing kinetic energy and an increasing elastically stored energy. Second, the evolution of the plastically stored energy W^p in figure 4c is also consistent with the observed response. Namely, an irreversible evolution until the elastic unloading and the incident plastic waves interact, followed by a purely elastic deformation and by a plastic reloading. However, the numerical results show some differences. Indeed, both MPM computations lead to higher plastically stored energies than that provided by FEM while DGMPM solutions yield a lower bound. This can be explained by the overshoots that can be seen in the central region, whose amplitude is more or less important depending on the method considered. Recall that this amplitude increases according to the following sequence of numerical solutions: MPM (1ppc), MPM(2ppc), DGMPM (2ppc), FEM, DGMPM (1ppc). The previous remark is consistent with the plastically stored energy plot in figure 4c, at least until the elastic evolution during which both DGMPM solutions get closer to each other. At last, the evolution of the total energy W^{TOT}, which is obtained by cumulating the incremental energy function (16) over the time steps, is depicted in figure 4d. The total energy is normalized with respect to its initial value W_0^{TOT} for all the numerical methods. Note that since the latter includes the pseudo-dissipation potential ϕ^*, the dissipation which can be observed is purely numerical. Thus, the figure shows that the total energy is pretty well conserved during every numerical simulation, although some slight differences due to the reasons already mentioned previously can be seen. In particular, the final values of the relative total energy are reported in table 3.

	FEM	DGMPM (1ppc)	DGMPM (2ppc)	MPM (1ppc)	MPM (2ppc)
$W^{\text{TOT}}(t = t_{\text{end}})/W_0^{\text{TOT}}$	99.37%	98.98%	98.12%	98.74%	98.93%

Table 3: Comparison of the final relative total energy for several numerical methods ($\beta = 1.2$).

Remark 5. *In comparison with the energy plots provided in [16] for the linear case (see figure 4.2), the use of the effective mass matrix highly reduces the numerical dissipation when more than one particle lies in the cells. However, it is worth noticing that this numerical trick is not well understood so far and requires further analyses.*

The loading parameter is now raised to $\beta = 4$ so that the small strain assumption no longer holds. Since no exact solution is available for that problem, finer meshes made of 300 finite elements and 300 material points are used so that the response of the medium can be satisfactorily identified and the numerical solutions can be compared. The numerical results in terms of longitudinal stress and plastic strain are depicted in figure 5. First, figure 5a shows the incident plastic wave along with the elastic precursor that propagate in the right half of the medium. The latter is reflected at the free boundary as an elastic unloading wave, as can be seen in figure 5b. The elastic wave is similarly captured by the FEM and the DGMPM(1ppc), while the three other solutions are smoother. As already mentioned, the finite element stress oscillates on the plastic plateau even with a fine mesh, which leads to overshoots in the plastic strain. Similarly to the previous loading case, MPM solutions are close to the DGMPM(2ppc) one on the elastic wave. However, it can now be seen that the MPM stresses and plastic strains are slightly sharper than both DGMPM results on the plastic wave. The two DGMPM solutions are, on the other hand, closer to each other on the plastic wave than in the previous loading case. Note also that the overestimation of the plastic strain in the central region of the medium still occurs in FEM, MPM and DGMPM(2ppc) solutions, though the latter is less pronounced. The two above dissimilarities with respect to the lower loading condition $\beta = 1.2$ in the DGMPM solutions are most likely due to the mesh refinement. Figures 5c and 5d next show that the interaction of the reflected elastic unloading wave with the incident plastic wave near the free end gives rise to a right-going elastic precursor followed by a plastic wave, as well as a left-going elastic unloading wave. Additional reflections thus occur at the free end, leading to two elastic waves followed by a plastic wave, propagating left-ward, the latter causing an increase in the longitudinal plastic strain. Slight differences between the numerical plastic strain can be seen in the right part of the medium, especially for the middle elastic wave in figure 5d. Nevertheless, the plastic strain profiles are rather close to each other, though the portion of the medium that underwent plastic loading in DGMPM is slightly smaller than in FEM and MPM ones. Then, a right-going elastic unloading wave coming from the middle of the solid, which can be seen in figure 5e, interacts with the left-going elastic wave (figure 5f) so that plastic reloading occurs. Owing to the overestimation of the plastic strain in FEM and MPM solutions in the central region, the results provided by these three approaches are rather late on DGMPM ones. The above observation is more obvious in figure 5g where a shift in the stress and

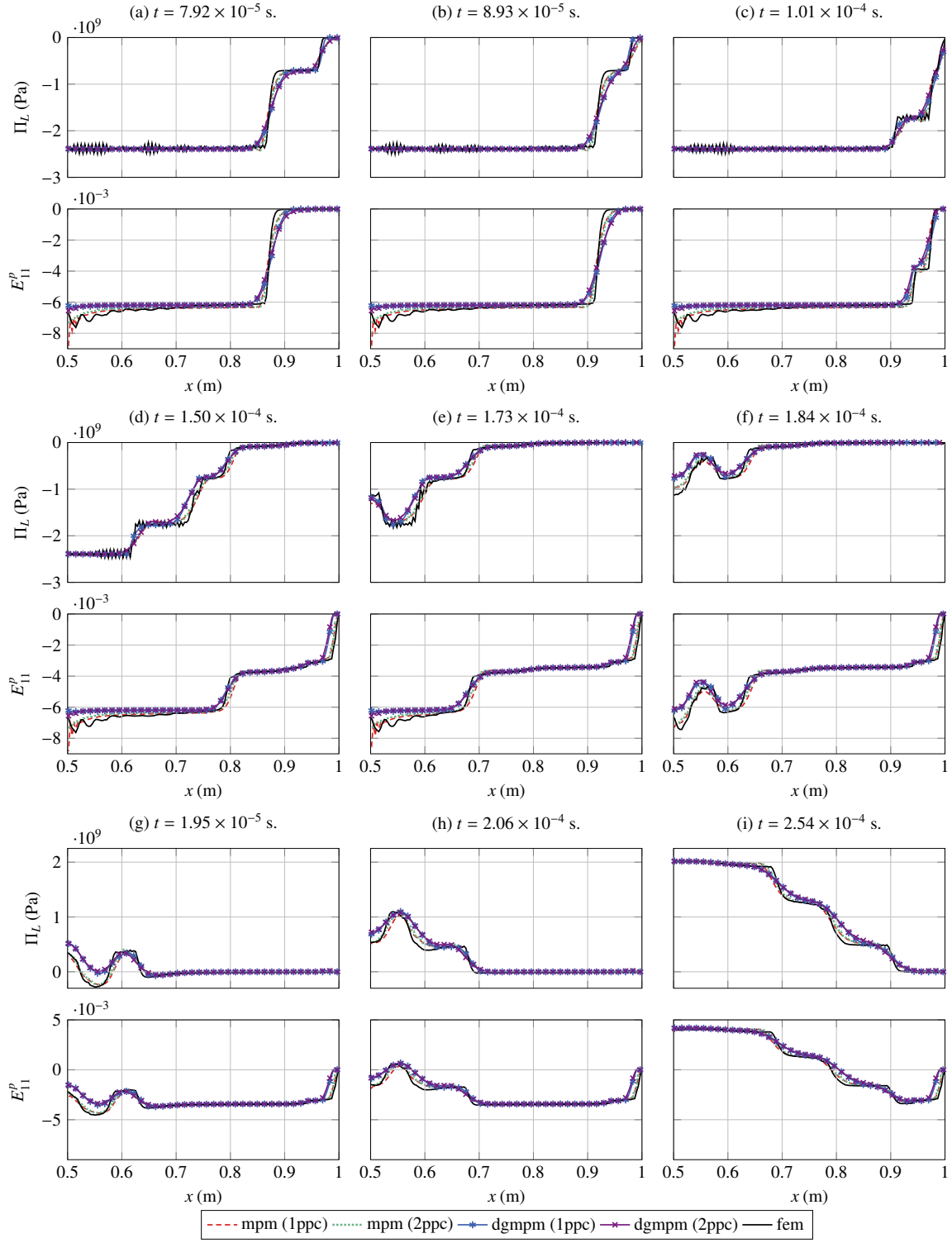

Figure 5: Stress and plastic strain profiles along a one-dimensional hyperelastic-plastic domain subject to Riemann-type initial conditions on the velocity at different times. Initial velocity set to $v_d = 4Y_H/\rho c_L$.

plastic strain values can be seen between DGMPM on the one hand, and the FEM and the MPM on the other hand. This gap reduces with time, as can be seen in figure 5h, so that the numerical results show good agreement with each other. Next, figure 5h shows that the multiple interactions of waves yield plastic tensile loadings in the central part of the medium. As a result, the computations end with three right-going plastic waves that can be seen in all numerical solutions in figure 5i.

The evolution of energy quantities is once again looked at. As before, the kinetic, the elastically stored, the

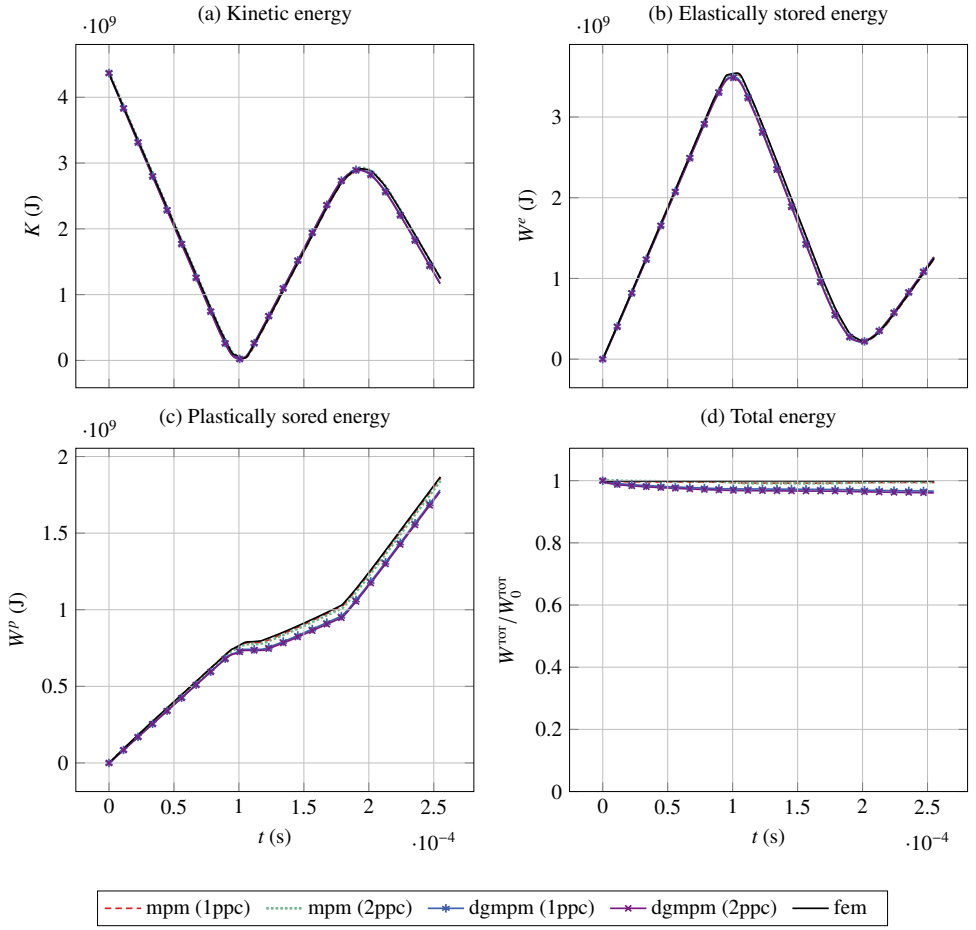

Figure 6: Evolution of energy quantities in the hyperelastic-plastic domain subject to Riemann-type initial conditions on the velocity at different times: comparison of all the numerical results. Initial velocity set to $v_d = 4Y_H/\rho c_L$.

plastically stored and the relative total energies are depicted versus time in figure 6. Figures 6a and 6b first show that the kinetic and elastically stored energies computed by all the numerical methods show good agreement. However, some differences appear on the plastically stored energy in figure 6c. Indeed, the finer mesh that has been used leads to FEM and MPM curves that are very close to each other, while DGMPM curves remain below them. This can be explained by the fact that the DGMPM is a first-order method only [2]. Nevertheless, the numerical dissipation exhibited by the method is not much higher than those of the second-order approaches, as shown by the results gathered in table 4.

6.2. Impact on a linear isotropic hardening material under plane strain

We now consider an infinite domain in the direction $\boldsymbol{e}_3$ with square section of length $l = 3m$. The left boundary of the section is normally fixed and a negative initial velocity is prescribed so that the problem can be seen as a plane strain version of the Taylor bar impact (see figure 7a). This setting is better suited to the testing of the DGMPM

	FEM	DGMPM (1ppc)	DGMPM (2ppc)	MPM (1ppc)	MPM (2ppc)
$W^{\text{TOT}}(t = t_{\text{end}})/W_0^{\text{TOT}}$	99.89%	96.63%	96.07%	99.43%	99.55%

Table 4: Comparison of the final relative total energy for several numerical methods ($\beta = 4$).

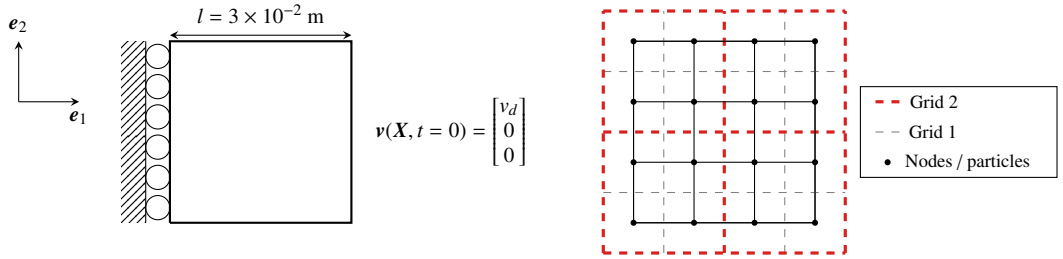

(a) Geometry and boundary conditions

(b) Material points set and grids

Figure 7: Geometry, loading and space discretizations used for the impact problem of a two-dimensional medium on a rigid wall. The initial velocity is set to $v_d = -300\, m/s$.

than the usual axisymetric Taylor bar, for the latter involves a geometric source term in system (4). This requires the employment of fractional-step methods such as Godunov's splitting [4], that come with their own stability restrictions [49].

The MPM and the DGMPM results are compared to two $Q1$-finite element (bilinear approximation) solutions coupled with a central difference explicit time integrator. The first one is based on a standard displacement-based formulation, while the second one makes use of a hybrid P0-P1 pressure-displacement mixed formulation, usually employed to avoid volumetric locking [3]. The domain is discretized such that the material points are equivalent to the finite element nodes: $l \times l \equiv 46 \times 46$ particles and nodes. Moreover, two arbitrary grids are used for the particle-based methods so that either one or four material points lie in every cell according to the situations depicted in figure 7b. This simulation enables comparisons between the numerical methods in spite of the lack of exact solution for that problem.

Comparisons in terms of the longitudinal stress Π_{11} and the cumulated plastic strain p are shown in the solid rotated anticlockwise of 90 degrees in figure 8. Notice that a mesh is reconstructed for MPM and DGMPM results for visualization purpose, and that the comparisons are made in the deformed configuration, before the first reflection and after the fourth one of the pressure wave in the medium respectively.

Before the first reflection of the pressure wave, the occurence of spurious oscillations in MPM and FEM solutions, though much slighter in the latter, leads to a different assessment of fields. On the other hand, the DGMPM solutions behave well and the method yields similar results with both distributions of material points. Then, figure 8b shows that the numerical cumulated plastic strains have globally the same shape but different extreme values. The maximum value of the cumulated plastic strain is given by the mixed FEM and occurs at the normally fixed end of the domain.

After four reflections of the incident waves, the solid is crossed by a left-going tensile wave, as shown in the second column of figure 8a. Similar observations as before can be made on the MPM stress solution, that is, significant oscillations. On the other hand, both FEM results are close from one to another, except at the left corners where the standard FEM leads to a higher amplitude of Π_{11}. Although the FEM and DGMPM stresses are quite similar before the first reflection, it is no longer the case due to the numerical dissipation inherent in the DGMPM. Furthermore, figure 8b shows that the plasticity continues propagating within the domain. The extreme value of the cumulated plastic strain computed with the standard FEM is higher than that of the mixed FEM. It is worth noticing that the MPM results show good agreement with the latter whereas the plastic flow has less developed in DGMPM ones. Moreover, some differences can be seen between the shapes of the solid provided by the numerical schemes.

We now propose to look at the above results in more details. Figures 9 and 10 show the evolution of the longitudinal stress and the cumulated plastic strain along the middle line ($x_2 = 1.5\,\text{cm}$) and the top half of the left end of the domain

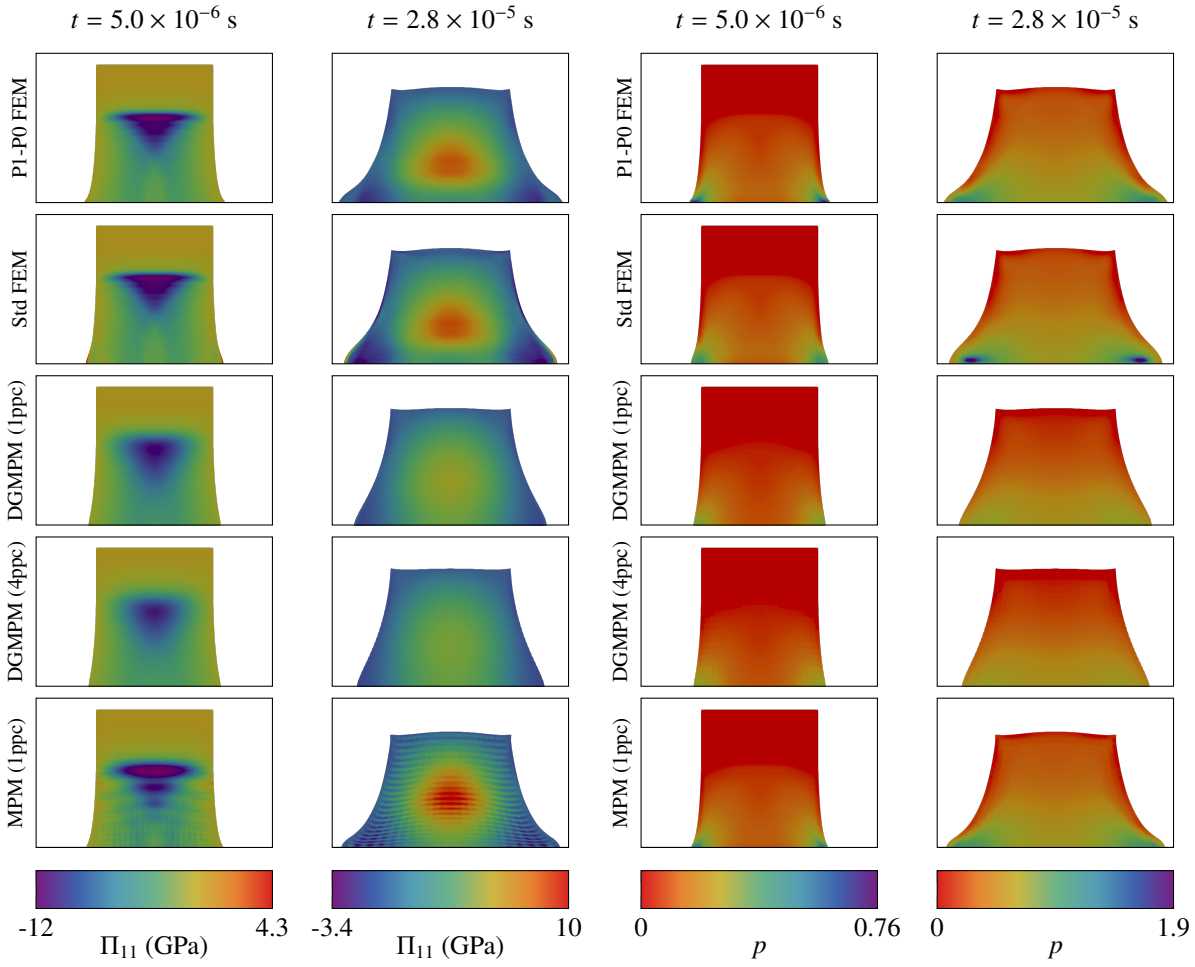

(a) PK1 stress component Π_{11}

(b) Cumulated plastic strain

Figure 8: Comparison between mixed and standard FEM, MPM (1ppc), DGMPM (1ppc and 4ppc) solutions for the plane strain Taylor bar problem.

respectively for the same time steps as before. First, it can be seen in figure 9a that the incident wave is described with different levels of sharpness by the numerical schemes. Then, the figure also shows the oscillations in the MPM stress solution already mentioned. Moreover, the superimposition of the stresses resulting from MPM computations using 1ppc or 4ppc shows that refining the particles discretization does not allow the removal of the numerical noise. In addition, it can be seen that the plastic strain plateau is not similarly computed by all the numerical methods and that smoother profiles are obtained with the particle-based approaches. Upstream the plastic front, the MPM and FEM plastic strains are close and higher than DGMPM ones. On the other hand, the two DGMPM results are close from one to another on the plastic plateau. After several reflections (figure 9b), the stress profiles are also different. The MPM still yields oscillating solutions regardless of the space discretization used and DGMPM results are slightly smoother than FEM ones. In spite of the significant oscillations, the MPM cumulated plastic strain profiles show good agreement with both FEM solutions which, in turn, are above these computed with the DGMPM. The last thing that can be seen in this figure is that the displacement of the right point, initially located at $x_1 = 3$ cm, is not the same for every numerical method. The previous observations are even more significant when looking at the evolution of fields along the top half of the left boundary (figure 10). In figure 10a, FEM, DGMPM and MPM(1ppc) stress profiles show good agreement, except at the top corner, while spurious oscillations pollute the MPM(4ppc) ones. Although

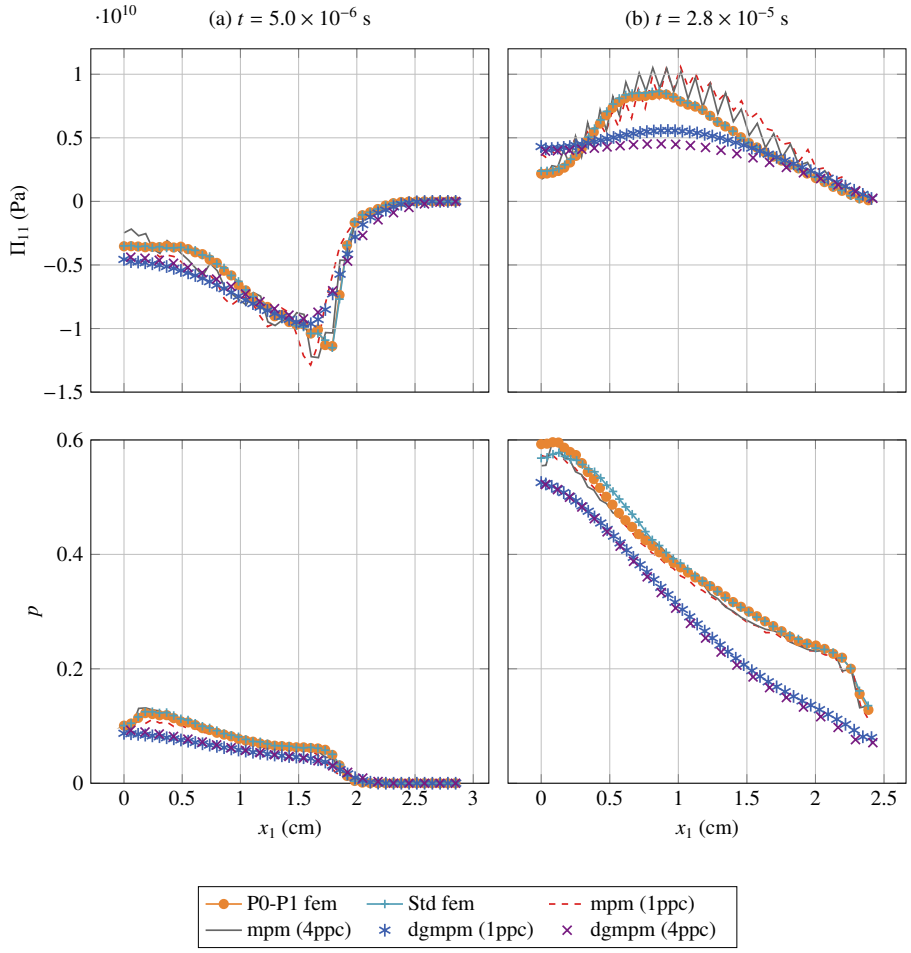

Figure 9: Comparison of the longitudinal stress component and cumulated plastic strain along the bottom boundary of the domain at two times.

FEM, DGMPM and MPM(1ppc) stresses are similar, it is not the case for the cumulated plastic strains, for which the numerical results differ more in the top part of the boundary. Thus, both FEM solutions yield the highest values of cumulated plastic strain at the top left corner of the domain. It can also be seen in that the corner point, initially located at $x_2 = 3$ cm, encourts a displacement that is more or less important depending on the numerical method.

The results depicted at the subsequent time still show that both MPM solutions oscillate so that the noise is not reduced by refining the particle distribution. On the other hand, DGMPM and FEM stresses are more different than before. Note also that the two FEM formulations lead to mismatched curves along that boundary. Moreover, the cumulated plastic strain curves show similar behaviors to those of the previous time step. Both DGMPM curves are below those computed with the FEM and the profiles resulting from MPM computations are less regular than the others. At last, the final shape of the domain is such that the lowest displacement amplitudes of the top corner are given by the DGMPM, while the highest is given by the mixed FEM, the MPM(1ppc) being close to the latter.

Given the differences mentioned above about the final shape of the solids, we now focus on the hydrostatic pressure: $\bar{\sigma} = \frac{1}{3}\,\text{trace}\,\boldsymbol{\sigma}$, where $\boldsymbol{\sigma}$ is the Cauchy stress tensor. Since no volumetric locking occur if the mixed FEM is used, only the MPM and DGMPM solutions are considered. In figure 11, the isovalues of the hydrostatic pressure are depicted in the deformed shapes resulting from the two MPM and DGMPM computations. Then, one can see that, as for the PK1 stress, the MPM hydrostatic pressures exhibit a checkerboard-like structure. It is worth noticing that this phenomenon is absent of DGMPM solutions in spite of the lower displacement observed, which suggests that volu-

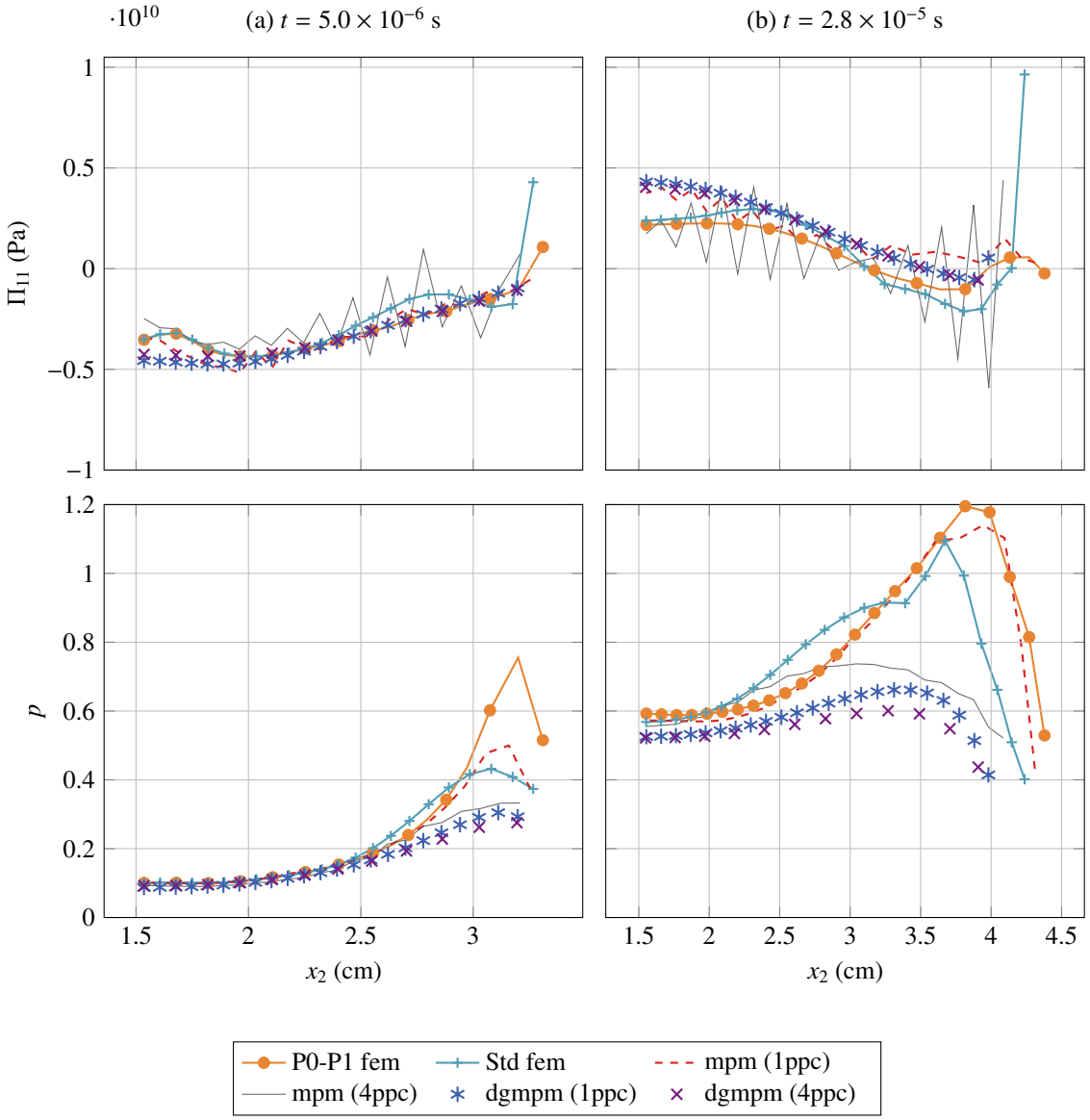

Figure 10: Comparison of the longitudinal stress component and cumulated plastic strain along the top half left boundary of the domain at two times.

metric locking occurs. The method might therefore be constructed upon an alternative hyperbolic system consisting of equations (1) and (2), supplemented with the conservation law for the Jacobian of the deformation $J = \det \boldsymbol{F}$ [10] to deal with plastic incompressibility.

6.3. Impact on a non-linear isotropic hardening material

Let consider again a square domain, acted upon a traction force on a part of its left end, as depicted in figure 12a. Moreover, the medium is assumed to be made of a non-linear isotropic hardening material following a power law as mentioned at the beginning of the section. The applied traction force on the left boundary domain gives rise to a compression pressure wave and a shear wave that propagate within the domain, the former being reflected on the right free end as an unloading wave. The external load is released at time $t_u = l/c_L$ as can be seen in figure 12b, which also

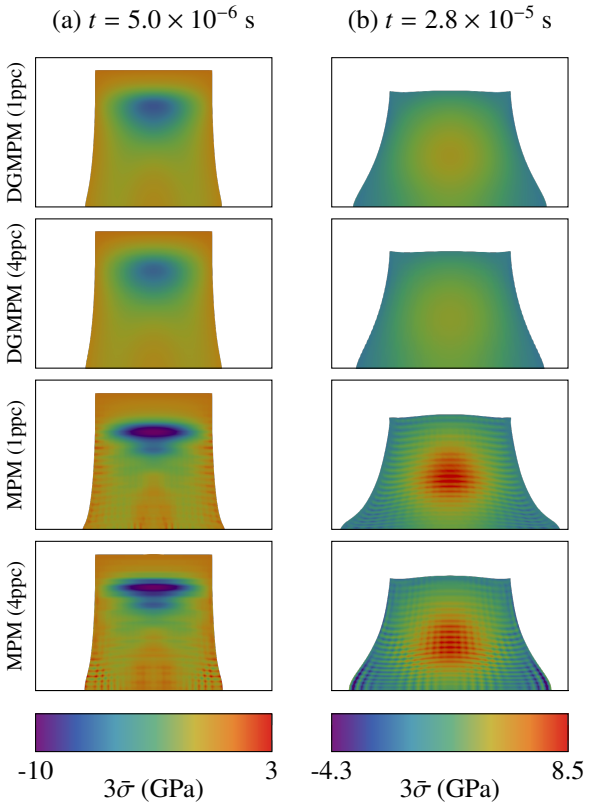

Figure 11: Isovalues of hydrostatic pressure in the two-dimensional hyperelastic-plastic solid. Comparison between, DGMPM and MPM solutions.

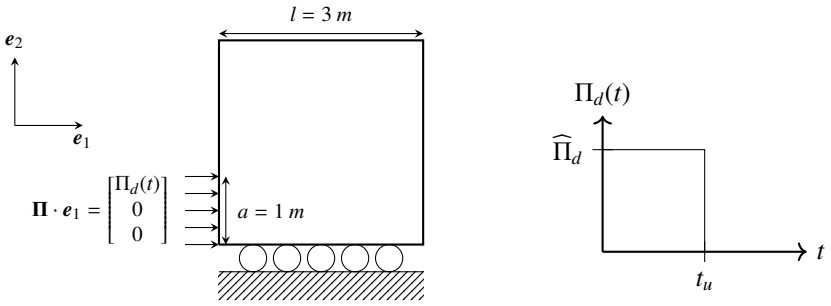

(a) Geometry and boundary conditions (b) Loading function

Figure 12: Geometry and loading for the impact problem on a two-dimensional medium. The external load $\widehat{\Pi}_d$ is set to 10GPa $\approx 14.3 Y_H$.

results in an unloading pressure wave. Both relaxations then interact so that tensile pressure waves propagate leftward and right-ward. Similar considerations are made for modeling the laser shock adhesion test [50], which aims at detecting adhesion defects at the interface between workpieces owing to the tensile wave resulting from the plasma-induced laser pulse. The purpose is here to illustrate the applicability of the DGMPM to an engineering problem whose simulation requires a precise tracking of waves. Comparisons are made between mixed FEM, MPM and DGMPM solutions computed in the square made of 46×46 particles and finite element nodes, on the longitudinal stress component Π_{11} (figure 13) and the cumulated plastic strain (figure 14). These figures allow a qualitative comparison

between the numerical results in the whole domain, proposed for the sake of completeness, and are supplemented with plots along the bottom boundary of the square in figure 15.

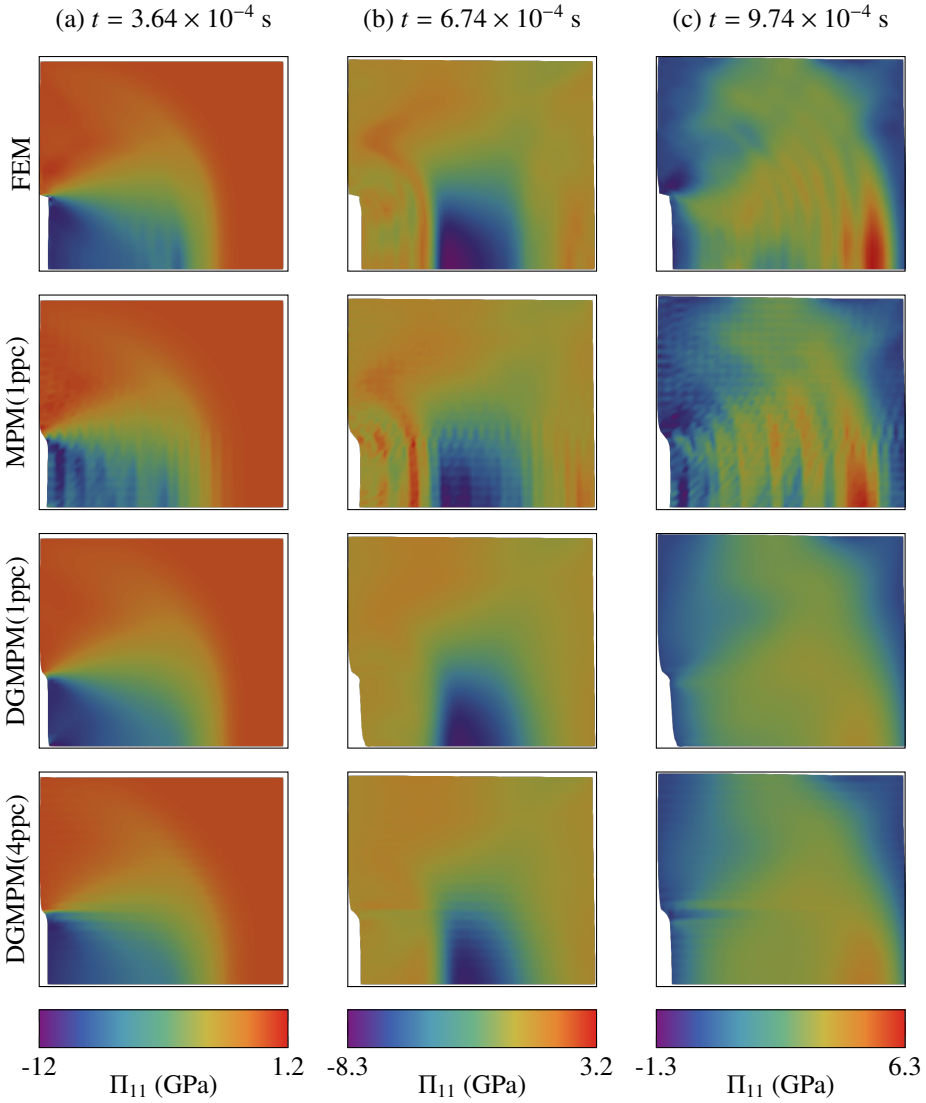

Figure 13: Isovalues of the stress component Π_{11} in a two-dimensional hyperelastic-plastic solids undergoing a dynamic stress pulse on its left end. Comparison between FEM, MPM(1ppc) and DGMPM solutions using either 1ppc or 4ppc.

First, the incident compression wave can be seen in figure 13a. As before, spurious oscillations occur in the MPM solution whereas the FEM and the DMPM well capture the right-going pressure wave. Nevertheless, the circular profile of the wave front due to Poisson's effect can be distinguished in every numerical solution. Figure 13b next shows the right-going and left-going unloading waves resulting respectively from the releasing of the external force, and from the reflection of the incident wave at the right end. Such a sudden relaxation of the loading leads to noisy FEM and MPM solutions while the phenomenon does not occur in DGMPM computations. Note also that a horizontal band appears in the FEM longitudinal stress due to the spatial discontinuity of the external load on the left end. After the interaction of the waves (figure 13c), two tensile pressure waves propagate towards both ends of the domain. As a result of the aforementioned colliding, more spurious oscillations are introduced within FEM and

MPM stresses. Contrariwise, the DGMPM is not perturbed and provides very satisfactory results with one or four

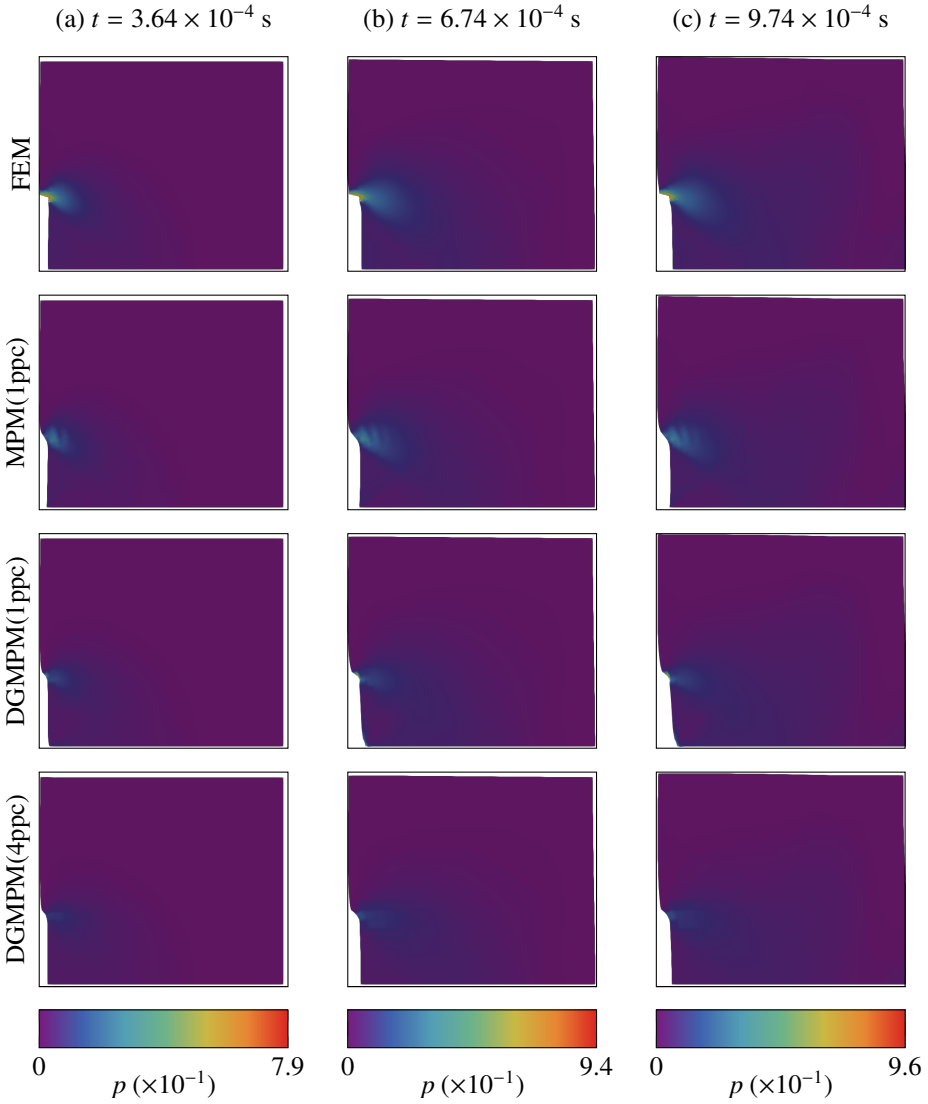

Figure 14: Comparison of the cumulated plastic strain p in the two-dimensional domain undergoing a compression impact on its left end.

particles per cell. Notice also that the final shape of the domain resulting from the four computations exhibit slight dissimilarities, especially close to the loaded region. These differences are most likely due to the shear induced by the spatial discontinuity in the applied load and should be reduced by considering a smoother profile $\Pi_d(x_2, t)$ on the left end.

We now move on to figure 14, in which the isovalues of the cumulated plastic strain are depicted at the same times as before. Figure 14a first shows the plastic flow resulting from the incident compression wave. Omitting the differences near the loaded boundary, which are caused by the spatial discontinuity of Π_d, the plastic flow develops rather identically in every numerical result. In figure 14b, the cumulated plastic strain no longer varies in the left part of the domain since the external pressure has been released at that time. The same goes for the very right part of the domain that is traversed by the reflected rarefaction wave. However, the material continues hardening close to the middle of the solid, where the two unloading waves are about to interact with each other. At last, the tensile waves

resulting from the aforementioned interaction of unloading waves yields, in figure 14c, a new plastic flow. The above remarks are more obvious when looking at the results along the bottom boundary in figure 15.

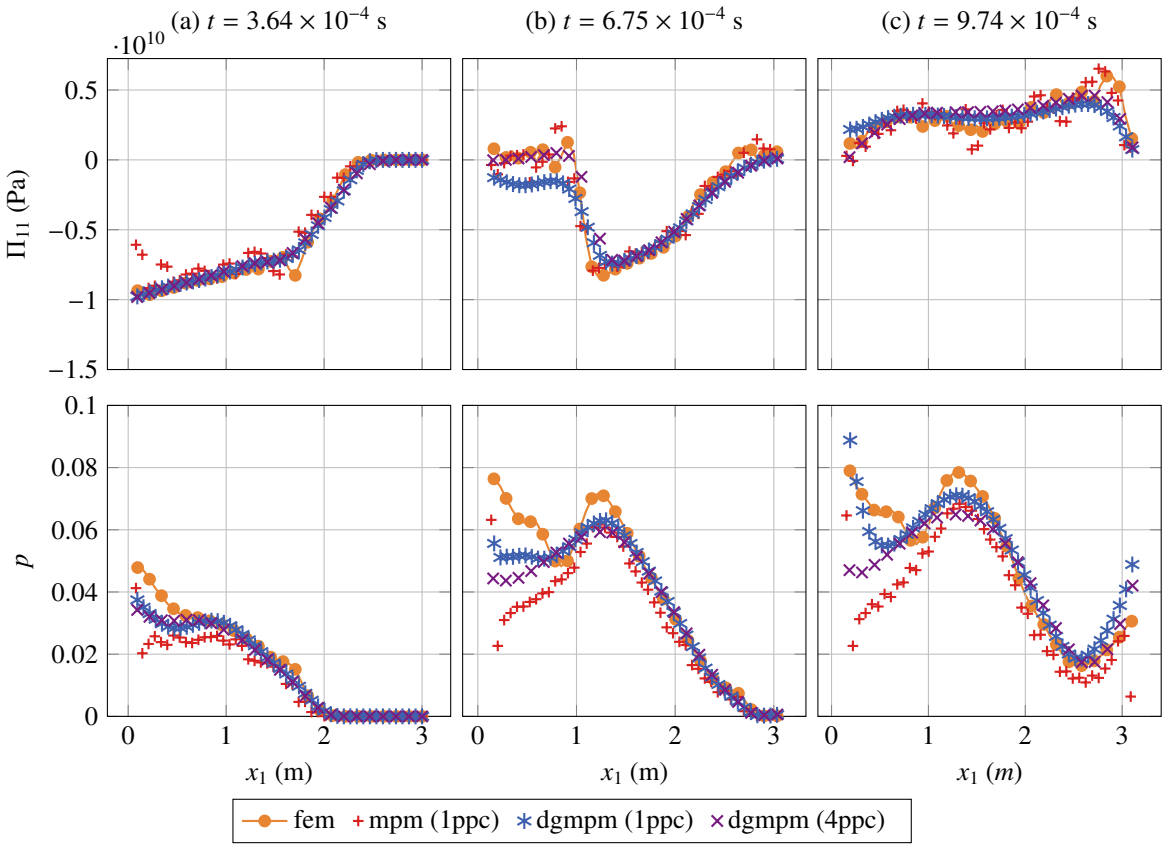

Figure 15: Evolution of the longitudinal stress component Π_{11} and the cumulated plastic strain p along the bottom boundary of the domain at several times.

In figure 15a, one can see that the numerical results are rather close from one to an other, up to some oscillations in the MPM solution at the left end. Furthermore, a little overestimation in the FEM stress leads to a slightly higher level of cumulated plastic strain near the middle of the bottom line. Given that the method is not monotone, this most likely corresponds to an overshoot due to the propagating shock.

On the other hand, the cumulated plastic strain is underestimated in the MPM(1ppc) solution in comparison with the DGMPM(4ppc) and the FEM. The MPM underestimates the cumulated plastic strain at the left corner, according to what is observed for the stress. Note also that at the left end, the cumulated plastic strains resulting from FEM, MPM and DGMPM differ. However, as for the simulation in section 6.2, the two DGMPM discretizations lead to close solutions. Similar observations can be made in figure 15b, which shows other overshoots arising in FEM and MPM stresses. The differences that were visible on the cumulated plastic strains at the left end have been accentuated by the releasing of the external load. In addition, the FEM leads to the lowest minimum value of the longitudinal stress which in turn, yields the highest cumulated plastic strain close to the middle of the boundary. At last, the profile of fields after the interaction of the unloading waves can be seen in figure 15c. The loading turned into a tensile state all along the bottom boundary, which leads to an increase in the cumulated plastic strain in the right part of the solid. Whereas DGMPM results remain very close from one to another far from the left end, additional oscillations occur in FEM and MPM solutions, so that different magnitude of tensile stress are visible with still some overshoots in the stresses.

These results again emphasize the importance of accurately capturing the waves. Indeed, considering the laser

shock adhesion test, the numerical methods used above might yield different conclusions. Even though the FEM is a second-order method in displacement that is proven to be very robust, overestimating stress and plastic strain, even locally as highlighted in the simulations considered here, may have consequences on the error made over the experimental data. On the other hand, such behaviors have not been seen for the DGMPM in spite of the youth of the method, which appears to be very promising.

7. Concluding remarks

The total Lagrangian formulation of the Discontinuous Galerkin Material Point Method has been applied to hyperelastic-plastic solids in this paper. The particle-based space discretization, combined with an arbitrary grid that is used as a support for the DG approximation, leads to the writing of an element-wise weak form of a hyperbolic conservation laws system. Integrations by part then give rise to boundary terms involving numerical fluxes calculated at the interfaces between the cells of the background mesh. These intercell fluxes can be computed by several ways including an approximate-state Riemann solver, whose construction has been presented. As for the Material Point Method, the solution of the discrete system on the background grid is used to update the fields that are stored at the particles and especially internal variables for history-dependent materials. The DGMPM has been here coupled to a variational constitutive integrator for the integration of the plastic flow.

The method has first been illustrated on a one-dimensional problem in a hyperelastic-plastic material involving the propagation of a plane wave. For low loading conditions, the DGMPM shows good agreement in terms of stress and plastic strain with the exact solution developed within the linearized geometrical framework. However, the solution can be more or less accurate depending on the space discretization since the stability properties of the scheme are known to be influenced by the number of particles lying in the elements of the background grid. The DGMPM has also been shown to behave well for more severe loadings as well as for two-dimensional problems, though the lack of reference solution must be highlighted. As a result, the combination of the Riemann solver to compute the fluxes and the particles to represent the geometry then appears to bring significant improvements to the original MPM so that waves can be followed in finite-deforming media without oscillations. Furthermore, the arbitrary grid constitutes a significant advantage over the finite element method that allows to employ mesh-adaption strategies with no need for additional projection of fields. The use of the DG framework also obviously enables to locally increase the approximation order, provided a consistent quadrature rule, which is the object of ongoing works. At last, the employment of the DGMPM for strongly thermo-mechanically coupled problems in solid dynamics can be considered owing to the thermodynamically-consistent constitutive update that has been combined with the method in this paper.

References

[1] A. Renaud, T. Heuzé, L. Stainier, A Discontinuous Galerkin Material Point Method for the solution of impact problems in solid dynamics, Journal of Computational Physics doi:10.1016/j.jcp.2018.05.001.

[2] A. Renaud, T. Heuz, L. Stainier, Stability properties of the Discontinuous Galerkin Material Point Method for hyperbolic problems in one and two space dimensions, International Journal for Numerical Methods in Engineering 121 (4) (2020) 664–689. doi:10.1002/nme.6239. URL https://onlinelibrary.wiley.com/doi/abs/10.1002/nme.6239

[3] T. Belytschko, W. K. Liu, B. Moran, K. Elkhodary, Nonlinear finite elements for continua and structures, 2nd Edition, John wiley & sons, 2014.

[4] R. J. Leveque, Finite volume methods for hyperbolic problems, Cambridge university press, 2002.

[5] X.-D. Liu, S. Osher, T. Chan, Weighted essentially non-oscillatory schemes, Journal of Computational Physics 115 (1) (1994) 200 – 212. doi:https://doi.org/10.1006/jcph.1994.1187.

[6] A. Harten, High resolution schemes for hyperbolic conservation laws, Journal of computational physics 49 (3) (1983) 357–393. doi:https://doi.org/10.1016/0021-9991(83)90136-5.

[7] C. H. Lee, A. J. Gil, J. Bonet, Development of a cell centred upwind finite volume algorithm for a new conservation law formulation in structural dynamics, Computers & Structures 118 (2013) 13–38.

[8] N. Favrie, S. Gavrilyuk, Dynamics of shock waves in elastic-plastic solids, in: ESAIM: Proceedings, Vol. 33, EDP Sciences, 2011, pp. 50–67.

[9] T. Heuzé, Lax–Wendroff and TVD finite volume methods for unidimensional thermomechanical numerical simulations of impacts on elastic-plastic solids, Journal of Computational Physics 346 (2017) 369 – 388.

[10] J. Haider, C. H. Lee, A. J. Gil, J. Bonet, A first-order hyperbolic framework for large strain computational solid dynamics: An upwind cell centred total lagrangian scheme, International Journal for Numerical Methods in Engineering 109 (3) (2017) 407–456.

[11] F. H. Harlow, The particle-in-cell method for numerical solution of problems in fluid dynamics, Proc. Symp. Appl. Math. 15. doi:10.1090/psapm/015/9942.

[12] D. Sulsky, Z. Chen, H. L. Schreyer, A particle method for history-dependent materials, Computer methods in applied mechanics and engineering 118 (1-2) (1994) 179–196.
[13] J. Brackbill, D. Kothe, H. Ruppel, Flip: A low-dissipation, particle-in-cell method for fluid flow, Computer Physics Communications 48 (1) (1988) 25 – 38. doi:https://doi.org/10.1016/0010-4655(88)90020-3.
[14] C. C. Hammerquist, J. A. Nairn, A new method for material point method particle updates that reduces noise and enhances stability, Computer Methods in Applied Mechanics and Engineering 318 (2017) 724 – 738. doi:https://doi.org/10.1016/j.cma.2017.01.035.
[15] W. Reed, T. Hill, Triangular mesh methods for the neutron transport equation, Los Alamos Report LA-UR-73-479.
[16] A. Renaud, The Discontinuous Galerkin Material Point Method: Application to hyperbolic problems in solid mechanics, Ph.D. thesis, École Centrale de Nantes (2018).
[17] J. C. Simo, T. J. Hughes, Computational inelasticity, Vol. 7, Springer Science & Business Media, 2006.
[18] M. Ortiz, L. Stainier, The variational formulation of viscoplastic constitutive updates, Computer Methods in Applied Mechanics and Engineering 171 (3) (1999) 419 – 444.
[19] E. Fancello, J. M. Vassoler, L. Stainier, A variational constitutive update algorithm for a set of isotropic hyperelasticviscoplastic material models, Computer Methods in Applied Mechanics and Engineering 197 (49) (2008) 4132 – 4148. doi:https://doi.org/10.1016/j.cma.2008.04.014.
[20] E. Fancello, J.-P. Ponthot, L. Stainier, A variational framework for nonlinear viscoelastic models in finite deformation regime, Journal of Computational and Applied Mathematics 215 (2) (2008) 400–408.
[21] Q. Yang, L. Stainier, M. Ortiz, A variational formulation of the coupled thermo-mechanical boundary-value problem for general dissipative solids, Journal of the Mechanics and Physics of Solids 54 (2) (2006) 401 – 424.
[22] L. Stainier, M. Ortiz, Study and validation of a variational theory of thermo-mechanical coupling in finite visco-plasticity, International Journal of Solids and Structures 47 (5) (2010) 705–715.
[23] D. P. Bertsekas, Nonlinear programming, Journal of the Operational Research Society 48 (3) (1997) 334–334.
[24] B. J. Plohr, D. H. Sharp, A conservative eulerian formulation of the equations for elastic flow, Advances in Applied Mathematics 9 (4) (1988) 481 – 499.
[25] J. Bonet, A. J. Gil, C. H. Lee, M. Aguirre, R. Ortigosa, A first order hyperbolic framework for large strain computational solid dynamics. part I: Total lagrangian isothermal elasticity, Computer Methods in Applied Mechanics and Engineering 283 (2015) 689 – 732.
[26] J. Trangenstein, P. Colella, A higher-order godunov method for modeling finite deformation in elastic-plastic solids, Communications on Pure and Applied Mathematics 44 (1991) 41–100.
[27] E. H. Lee, Elastic-plastic deformation at finite strains, Journal of applied mechanics 36 (1) (1969) 1–6.
[28] J. Lubliner, On the thermodynamic foundations of non-linear solid mechanics, International Journal of Non-Linear Mechanics 7 (3) (1972) 237 – 254. doi:https://doi.org/10.1016/0020-7462(72)90048-0.
[29] C. Truesdell, W. Noll, The non-linear field theories of mechanics, 3rd Edition, Springer, 2004.
[30] D. Sulsky, S.-J. Zhou, H. L. Schreyer, Application of a particle-in-cell method to solid mechanics, Computer Physics Communications 87 (1-2) (1995) 236 – 252.
[31] D. A. Di Pietro, A. Ern, Mathematical aspects of discontinuous Galerkin methods, Vol. 69, Springer Science & Business Media, 2011.
[32] E. Love, D. Sulsky, An unconditionally stable, energy-momentum consistent implementation of the material-point method, Computer Methods in Applied Mechanics and Engineering 195 (33 - 36) (2006) 3903 – 3925.
[33] D. Burgess, D. Sulsky, J. Brackbill, Mass matrix formulation of the flip particle-in-cell method, Journal of Computational Physics 103 (1) (1992) 1–15.
[34] B. Cockburn, Discontinuous galerkin methods for convection-dominated problems, in: High-order methods for computational physics, Springer, 1999, pp. 69–224.
[35] S. Osher, Riemann solvers, the entropy condition, and difference, SIAM Journal on Numerical Analysis 21 (2) (1984) 217–235.
[36] R. Courant, D. Hilbert, Methods of mathematical physics [Methoden der mathematischen Physik, engl.] 1, CUP Archive, 1965.
[37] E. F. Toro, Riemann solvers and numerical methods for fluid dynamics: a practical introduction, Springer Science & Business Media, 2013.
[38] A. L. Ortega, M. Lombardini, D. Pullin, D. Meiron, Numerical simulation of elastic-plastic solid mechanics using an eulerian stretch tensor approach and hlld riemann solver, Journal of Computational Physics 257 (2014) 414 – 441. doi:https://doi.org/10.1016/j.jcp.2013.10.007.
[39] S. K. Godunov, Finite difference method for numerical computation of discontinuous solutions of the equations of fluid dynamics, Matematicheskii Sbornik 47(89) (3) (1959) 271–306.
[40] X. Lin, J. Ballmann, A riemann solver and a second-order godunov method for elastic-plastic wave propagation in solids, International Journal of Impact Engineering 13 (3) (1993) 463 – 478.
[41] J.-B. Cheng, Y. Jia, S. Jiang, E. F. Toro, M. Yu, A second-order cell-centered lagrangian method for two-dimensional elastic-plastic flows, Communications in Computational Physics 22 (5) (2017) 1224–1257. doi:10.4208/cicp.OA-2016-0173.
[42] P.-H. Maire, R. Abgrall, J. Breil, R. Loubre, B. Rebourcet, A nominally second-order cell-centered lagrangian scheme for simulating elastic-plastic flows on two-dimensional unstructured grids, Journal of Computational Physics 235 (2013) 626 – 665. doi:https://doi.org/10.1016/j.jcp.2012.10.017.
[43] P. Colella, Multidimensional upwind methods for hyperbolic conservation laws, Journal of Computational Physics 87 (1) (1990) 171–200.
[44] L. Stainier, Consistent incremental approximation of dissipation pseudo-potentials in the variational formulation of thermo-mechanical constitutive updates, Mechanics Research Communications 38 (4) (2011) 315–319. doi:10.1016/j.mechrescom.2011.03.011.
[45] Z. Więckowski, S.-K. Youn, J.-H. Yeon, A particle-in-cell solution to the silo discharging problem, International Journal for Numerical Methods in Engineering 45 (9) 1203–1225.
[46] Z. Więckowski, The material point method in large strain engineering problems, Computer methods in applied mechanics and engineering 193 (39) (2004) 4417–4438.
[47] J. Li, Y. Hamamoto, Y. Liu, X. Zhang, Sloshing impact simulation with material point method and its experimental validations, Computers & Fluids 103 (2014) 86 – 99. doi:https://doi.org/10.1016/j.compfluid.2014.07.025.
[48] S. Bardenhagen, E. Kober, The generalized interpolation material point method, Computer Modeling in Engineering and Sciences 5 (6) (2004) 477–496.

[49] U. M. Ascher, L. R. Petzold, Computer methods for ordinary differential equations and differential-algebraic equations, Vol. 61, Siam, 1998.
[50] L. Berthe, M. Arrigoni, M. Boustie, J. P. Cuq-Lelandais, C. Broussillou, G. Fabre, M. Jeandin, V. Guipont, M. Nivard, State-of-the-art laser adhesion test (LASAT), Nondestructive Testing and Evaluation 26 (3-4) (2011) 303–317. doi:10.1080/10589759.2011.573550.